

Demonstration of Super-X divertor exhaust control for transient heat load management in compact fusion reactors

Received: 9 September 2024

Accepted: 2 July 2025

Published online: 5 September 2025

 Check for updates

B. Kool^{1,2}✉, K. Verhaegh^{2,3}✉, G. L. Derks^{1,2}, T. A. Wijkamp^{1,2}, J. T. W. Koenders^{1,2}, N. Lonigro^{3,4}, G. McArdle³, C. Vincent³, J. Lovell⁵, S. S. Henderson³, F. Federici⁵, D. Brida⁶, H. Reimerdes⁷, N. Osborne^{3,8}, M. van Berkel¹, The EUROfusion Tokamak Exploitation Team* & the MAST-U team

Nuclear fusion could offer clean, abundant energy. However, managing the power exhausted from the core fusion plasma towards the reactor wall remains a major challenge. This is compounded in emerging compact reactor designs promising more cost-effective pathways towards commercial fusion energy. Alternative Divertor Configurations (ADCs) are a potential solution. In this work, we demonstrate exhaust control in ADCs, employing a novel method to diagnose the neutral gas buffer, which shields the target. Our work on the Mega Ampere Spherical Tokamak Upgrade shows that ADCs tackle key risks and uncertainties for fusion energy. Their highly reduced sensitivity to perturbations enables active exhaust control in otherwise unfeasible situations and facilitates an increased passive absorption of transients, which would otherwise damage the divertor. We observe a strong decoupling of each divertor from other reactor regions, enabling near-independent control of the divertors and core plasma. Our work showcases the real-world benefits of ADCs for effective heat load management in fusion power reactors.

Nuclear fusion has the potential to provide virtually limitless, inherently safe and clean energy¹. The most mature configuration, the tokamak², magnetically confines plasma particles in a torus-shaped device (Fig. 1a). However, the core power, carried by the plasma particles, eventually propagates outside the magnetically confined region and is compressed into a narrow region of open magnetic field lines, resulting in an immense heat flux^{3,4} akin to a welding torch. To prevent this heat flux from reaching the main chamber wall, it is diverted to a dedicated region (the divertor; Fig. 1a) using coils to create a magnetic

field ‘null’. A key issue for reactor-scale devices is that the resulting divertor heat load far exceeds material limits if not mitigated^{3,4}. As these loads are not only static but also change dynamically, the mitigation of transients is critical.

Compact, high magnetic field devices such as the Affordable Robust Compact reactor (ARC)⁵, Smallest Possible ARC (SPARC)⁶ and the Spherical Tokamak for Energy Production (STEP)^{7–10} promise a more cost-effective and faster route to commercial fusion energy¹¹. However, the decreased volume per unit power results in a substantially

¹DIFFER–Dutch Institute for Fundamental Energy Research, Eindhoven, the Netherlands. ²Eindhoven University of Technology, Eindhoven, the Netherlands.

³United Kingdom Atomic Energy Authority–Culham Campus, Culham, UK. ⁴York Plasma Institute, University of York, York, UK. ⁵Oak Ridge National Laboratory, Oak Ridge, TN, USA. ⁶Max-Planck-Institut für Plasmaphysik, Garching, Germany. ⁷École Polytechnique Fédérale de Lausanne (EPFL), Swiss Plasma Center (SPC), Lausanne, Switzerland. ⁸University of Liverpool, Liverpool, UK. *Lists of authors and their affiliations appear at the end of the paper.

✉e-mail: b.kool@differ.nl; k.h.a.verhaegh@tue.nl

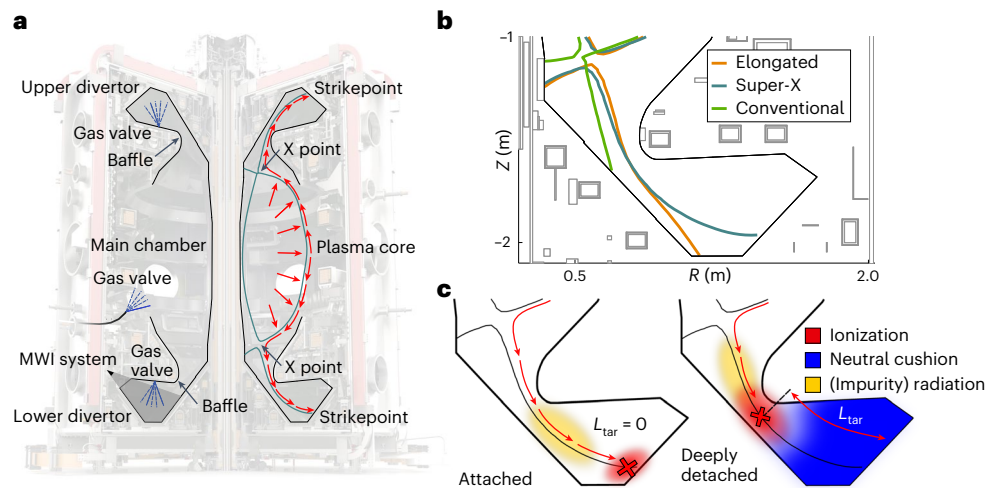


Fig. 1 The MAST-U tokamak, its divertor configurations and detachment.

a, MAST-U vessel with the gas valve and MWI¹⁴ locations indicated, the transport of energetic core particles towards the outer divertor targets is indicated by the red arrows. **b**, Cross-section of the lower divertor, using radial (R) and vertical (Z) coordinates, showing the wall, magnetic coils and the magnetic equilibria of the Super-X, Elongated and Conventional divertor configurations. **c**, Schematic of

an attached divertor (left) with volumetric impurity radiation and an ionization region located at the strikepoint ($L_{\text{tar}} = 0$), a detached ($L_{\text{tar}} > 0$) divertor (right) absorbs the incoming heat flux by forming a neutral cushion, massively reducing the strikepoint heat flux. Credit: background image in **a**, United Kingdom Atomic Energy Authority.

increased heat and particle load per area, exacerbating the heat exhaust challenge^{12,13}, which is already daunting for large devices such as ITER³ and the demonstration power plant (DEMO)⁴.

In a divertor, the plasma heat flux can be reduced by orders of magnitude by converting plasma energy flux (directed primarily along field lines) into photons and neutrals (not held by the magnetic field), spreading the heat flux over a larger area (Fig. 1c). This is achieved by injecting impurity and/or hydrogenic gases, dissipating the majority of the power (~75%) (refs. 14–16) in a ‘radiative region’ upstream of the ion source. The ion source initially remains attached at the target ($T_e > 3–5$ eV), higher gas injection rates lead to a detached ion source ($T_e < 3–5$ eV). This builds a cushion of neutral atoms and molecules above the strikepoint, enabling further power removal to ultimately ensure the required order-of-magnitude heat flux reduction.

Insufficient gas injection results in inadequate dissipation and, consequently, insufficient divertor protection. Conversely, excessive gas injection can drive the cold, detached, region into the core plasma, reducing core performance^{17–19} and potentially damaging the reactor through a violent plasma termination¹⁸. The challenge of maintaining this balance is exacerbated by transients originating from plasma core instabilities², core pellet fuelling²⁰ and power-sharing imbalances between divertor targets^{10,21}. The resulting cyclic power loading can lead to a loss of stable detachment and therefore divertor tile cracking²². Active power exhaust control is thus imperative for reactor-scale devices to maintain the ‘right’ balance^{4,8,19,23,24} in both attached and detached conditions.

Recent progress in exhaust control has been achieved using conventional divertors, employing diagnostics based on impurity emissions location^{19,25}, radiated power^{26–29}, tile temperature³⁰, plasma temperature³¹, ion target flux³² and tile current³³. However, active control can only mitigate transients slow enough for gas actuators to respond, faster transients must be absorbed passively, an inherently limited capability. It therefore remains uncertain if conventional divertors can effectively manage the power exhaust challenge^{17,34}, posing a major risk for fusion power reactors.

Several alternative exhaust solutions are being explored as a risk-mitigation strategy, including liquid metal divertor targets³⁵, highly radiative plasma regimes³⁶ and Alternative Divertor Configurations (ADCs)^{17,34}. These configurations rely on plasma shaping to improve power exhaust, detachment access and its control^{17,34}.

Whereas ADCs are investigated as a risk-mitigation strategy for DEMO, they are an absolute necessity for compact reactors. However, ADCs increase engineering complexity, divertor volume and therefore cost (Methods)^{34,37}. Any reactor implementation has to carefully consider the trade-off between these drawbacks and the attractive operating regimes ADCs offer.

One of the most promising ADCs is the Super-X Divertor (SXD) (Fig. 1a,b), featuring an increased strikepoint major radius, increasing the target area. Under steady-state conditions, massively reduced target heat and particle fluxes with an improved access to detachment have been observed^{14–16}, consistent with reduced model predictions²³ and simulations^{38,39}.

The Mega Ampere Spherical Tokamak in the UK was recently upgraded (MAST-U)^{40,41} (Extended Data Fig. 1) to facilitate long-legged ADCs. It features a large divertor volume to explore various ADCs, including the SXD. Less extreme configurations such as the Elongated Divertor (ED) (Fig. 1b) can also be achieved and are potentially easier to integrate in a reactor (Fig. 8). The ADCs are uniquely integrated with strong baffling to reduce the escape of divertor neutrals towards the core^{38,42}. It features an up/down symmetric double-null geometry for improved power distribution^{10,13,34,43}.

In this work, we experimentally demonstrate real-time exhaust control in ADCs, employing the ED and SXD divertor configurations (Fig. 1b). This presents a drastically different situation compared to the single-null, conventional geometries employed previously^{19,25–33}. Our experiments feature a double-null, strong baffling and a 2× increase in total magnetic flux expansion¹⁶. We directly control the ionization front location in real time, and thereby detachment state, by diagnosing D₂ Fulcher emissions from excited molecules^{14–16}. This work proves that ADCs are compatible with exhaust control systems, a requirement for their implementation in fusion power reactors. We also showcase their capability to passively absorb transients, a major advantage in addressing the heat exhaust problem. Our results also show that the upper and lower divertors are largely decoupled, suggesting that both divertors can be near independently controlled. This fulfils a crucial requirement for double-null reactor designs to compensate transients originating from power-sharing asymmetries¹⁰. The implications of the ADC benefits for power exhaust control are discussed and we demonstrate the scalability of our detachment sensor strategy to reactors on a scientific, conceptual level, focusing on STEP^{7–10}. This pioneering

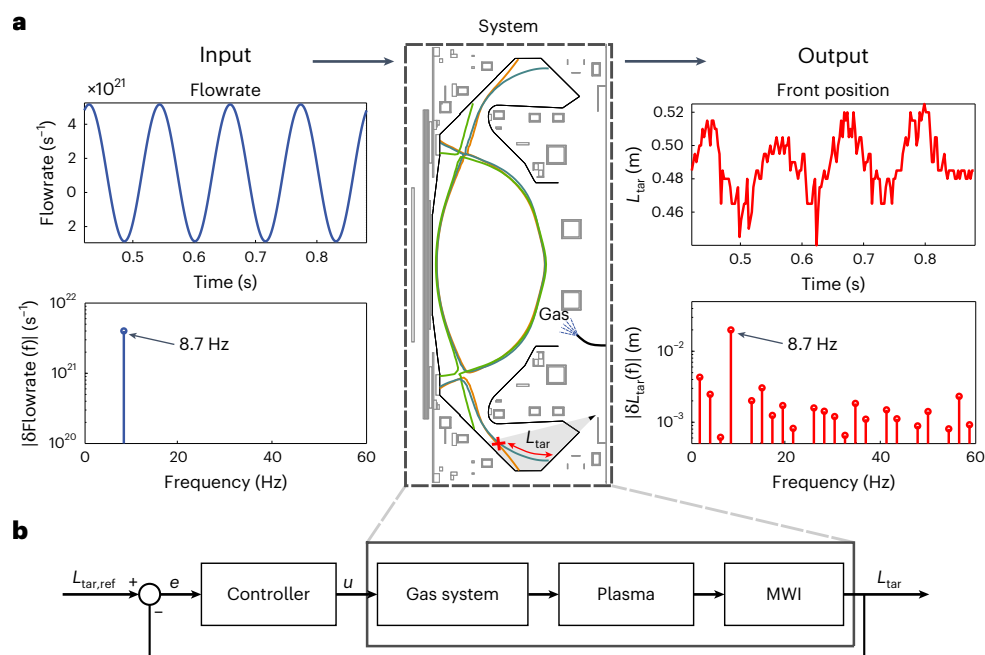


Fig. 2 | System identification and the feedback control loop. a, Time domain and frequency domain response of the D_2 Fulcher band front position L_{tar} to a perturbation of the requested main chamber D_2 gas valve flow rate in Super-X divertor geometry, experiment number 47116. The input frequency component is clearly observed in the system output; Extended Data Fig. 2. **b**, Feedback-

control loop showing the reference front position $L_{tar,ref}$, the error e with respect to the measured front position L_{tar} and the corresponding requested flow rate u by the controller. The to-be-controlled system includes the gas system, plasma and MWI sensor dynamics.

experimental work presents major progress towards addressing a key challenge for realizing fusion energy.

Dynamics of ADCs

In our experimental results, we observe major advantages of ADCs for solving the fusion exhaust challenge.

First, the divertor dynamics are studied to investigate the capability of handling transients. We systematically identify the detachment input–output dynamics, as recently demonstrated for conventional divertors^{19,25}. In these experiments, the divertor response to D_2 gas inflow perturbations is measured to identify the dynamics. We employ a (low-field side) main chamber D_2 gas valve, using a low-confinement mode (L-mode) scenario with 1.5-MW Neutral Beam Injection heating and core electron densities of $2\text{--}6 \times 10^{19}$ (m^3) (Methods). Using a novel ionization front-tracking technique, we perform a pioneering study of the detachment front dynamics in alternative divertor configurations in MAST-U.

The detachment state is tracked using the D_2 Fulcher emissions front location, defined as the position with 50% intensity extinction from maximum, as a proxy for the ionization front¹⁵ using the lower divertor Multi-Wavelength-Imaging (MWI)⁴⁴ camera system (Fig. 1a). In post-processing, the images are inverted⁴⁵ to obtain a 2D emissivity distribution, allowing the distance between target and ionization front along the divertor leg to be quantified⁴⁵ as L_{tar} (Fig. 1c) ($L_{tar} > 0$ during detachment; Methods). For comparison, we conduct conventional divertor (CD) experiments using an additional X-point camera system not available in the earlier ED and SXD experiments (Methods).

By analysing the frequency response of L_{tar} , the detachment front dynamics are retrieved. The perturbation signals are especially designed considering experimental constraints (Methods). The considered system includes the gas system dynamics, plasma response and MWI camera and is conceptually illustrated in Fig. 2. Because only the requested gas valve flow rate can be perturbed, the gas system dynamics cannot be separated from the detachment dynamics⁴⁶ (Methods). A typical time and frequency domain response is shown in Fig. 2 (Extended Data Fig. 2). We observe that the response on non-excited

frequencies mostly stays below the average noise level, with exceptions attributed to the gas system, not the plasma dynamics themselves (Methods). This indicates dominantly linear dynamics⁴⁷. Crucially, this implies that standard, linear control techniques are also suitable for these ADCs, akin to conventional configurations^{19,25}.

Comparing the dynamical response of the three divertor configurations (Fig. 3) shows that the ED and SXD have a much greater capacity to passively absorb transients and feature a reduced detachment onset threshold. In contrast, the CD requires much higher flow rates ($5 \times 10^{21} D_2 s^{-1}$) and line-averaged core densities ($5 \times 10^{19} m^{-3}$ vs $3 \times 10^{19} m^{-3}$) to detach, whereas the ED and SXD are already detached at the lowest flow rate needed for stable core conditions ($1 \times 10^{21} D_2 s^{-1}$) (Fig. 3a, showing $L_{tar} > 0$ for the ED and SXD). When the ionization front starts to detach from the strikepoint in the conventional divertor ($L_{tar} > 0$), it moves outside the divertor within 2.5 ms, to above the X point, resembling Multifaceted Asymmetric Radiation from the Edge⁴⁸. This persists until the end of the experiment, even though the fuelling is subsequently reduced (Extended Data Fig. 3). The observed transition from attached to above the X point indicates a very narrow operational window, that is, only a very limited range of gas flow rates would position the front in between target and X point, leading to a much more pronounced response to fuelling perturbations.

This is in stark contrast with both the SXD and ED divertors, where the response to the perturbations is only minimal (limited L_{tar} variation). The combination of this decreased sensitivity and increased divertor leg length entails that these ADCs have a much larger capacity to passively absorb transients and therefore avoid re-attachment and a radiative core plasma collapse. These findings are consistent with previous steady-state observations^{14–16} of a reduced detachment onset and front sensitivity for ADCs; our results now illustrate that these benefits extend to a dynamic situation.

As the ionization front in CD configuration is either attached or outside the divertor for most datapoints, only the dynamics for the ED and SXD configurations can be identified. The linear dynamics of the ED (*) and SXD (◇) configurations around the operating

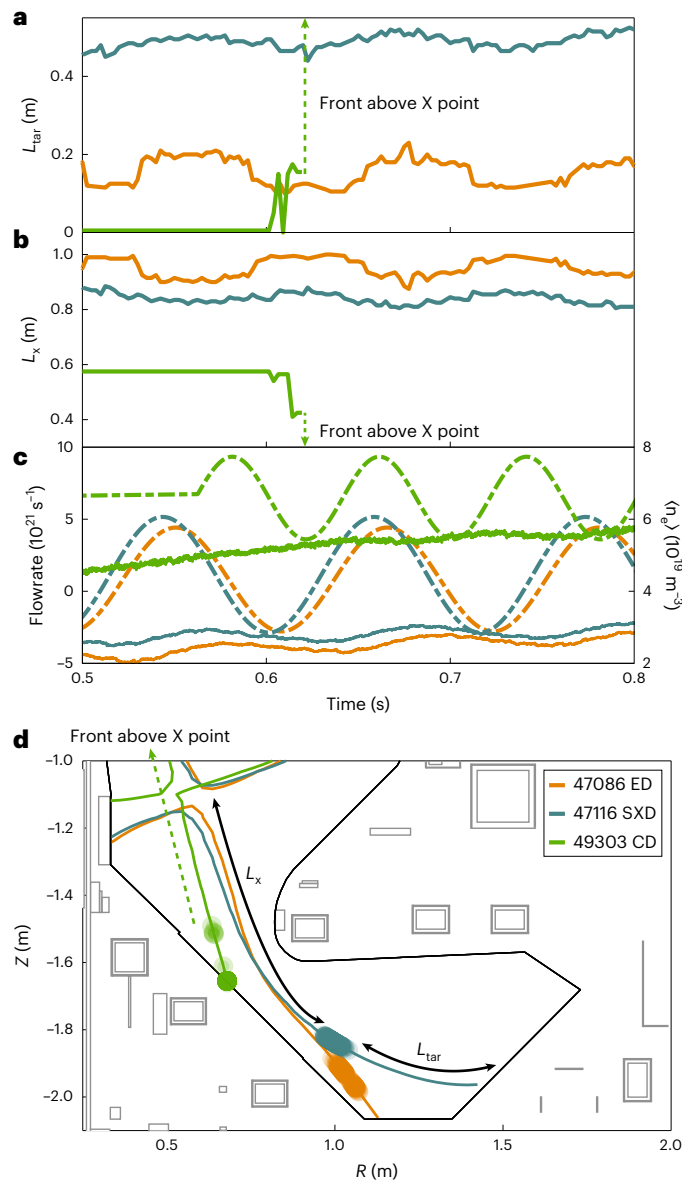


Fig. 3 | Comparison of Super-X, Elongated and Conventional divertor front movement. **a**, Divertor detachment state expressed as the distance of the Fulcher band front position to target along the divertor leg L_{tar} . **b**, D_2 Fulcher front position as the Poloidal distance between the D_2 Fulcher emission front and the X point L_x . **c**, Requested main chamber gas flow rate (left, -) and line-averaged core electron density (right, -). The requested gas flow rate is negative due to the inaccuracies in the gas valve calibration; Methods. **d**, Two-dimensional view of the magnetic configurations with an overlay of the front position at each timestamp within the time frame.

point can be expressed as a frequency response function (FRF) by analysing the input–output ratio in frequency domain (Fig. 4). We use the local-polynomial method⁴⁹ (LPM) to correct for transient effects and estimate 2σ error bars⁴⁷ (Methods). Across all measurements, we observe a 40° to 70° phase delay in the considered 7.7–38.5-Hz frequency range, notably less than the reported 70° to 140° in core density response⁴⁶. This suggests that the response can be modelled as a fractional differential equation, as observed for conventional divertors in the Tokamak à configuration variable (TCV)^{19,25}. The SXD and ED divertor configurations show a similar phase response, however, the SXD magnitude response is smaller compared to the ED (Fig. 3 and 4), suggesting a potential additional reduction in front sensitivity for the SXD.

We also consider the response of the main chamber D_{α} filterscope (Extended Data Figs. 4 and 5), capturing neutral hydrogen Balmer-alpha emissions as a key measure of plasma-neutral interaction. It is the most direct measurement available for when the injected gas reaches the plasma as it directly views the gas inlet. As a 30° to 90° phase delay is observed, the gas system itself might be a dominant source of the observed dynamics, underlining the importance of gas system dynamics for exhaust control. A complete understanding of the observed divertor dynamics is still lacking, requiring further investigation across multiple devices.

This marks experimental confirmation of the benefits of ADCs in passively handling dynamic transients, extending previous results for steady-state conditions^{23,38,39}. In addition to demonstrating the benefits of ADCs for solving the exhaust challenge in fusion power reactors, our results also enable feedback exhaust control in MAST-U through the systematic design of an exhaust controller.

Feedback control

We will now demonstrate that ADCs are compatible with exhaust control, a requirement for their application in fusion power reactors^{4,19,23,24}.

By matching a dynamic model to the measurements (Fig. 4), detachment control is enabled without explicitly modelling the intricacies of the underlying physical processes. We opt for a simple fractional order transfer function $G(j\omega)$, with gain $K = 10^{-22}$ (-), time constant $\tau = 0.3715$ (s), time delay $\tau_d = 10^{-3}$ (s) and frequency ω (rad s^{-1}),

$$G(j\omega) = \frac{K}{(\tau j\omega)^{0.7} + 1} e^{-\tau_d j\omega} \quad (1)$$

Using $G(j\omega)$, we design a basic Proportional-Integral (PI) controller $C(j\omega)$ through the loopshaping method⁵⁰ as

$$C(j\omega) = K_p + \frac{K_i}{j\omega}, \quad (2)$$

with proportional and integral gains as $K_p = 5 \times 10^{22}$ and $K_i = 3 \times 10^{24}$, respectively. The controller is targeted towards robustness for this proof of concept demonstration, evidenced by the low closed-loop

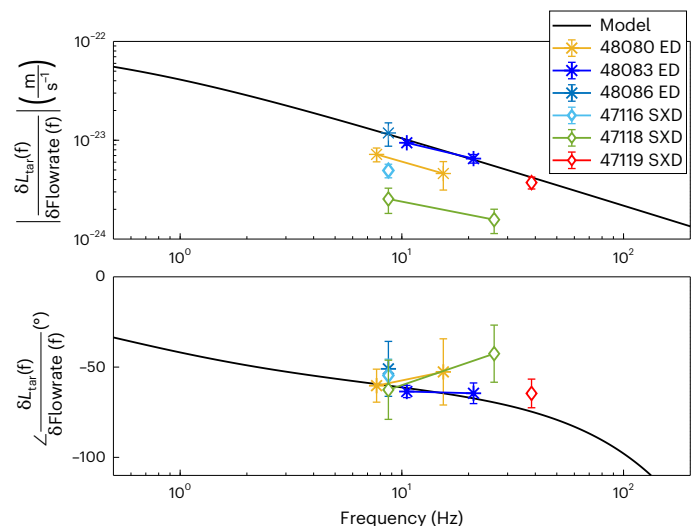


Fig. 4 | Detachment front frequency response. Requested main chamber gas valve flow rate change to Fulcher band front position response δL_{tar} in Elongated (*) and Super-X (◇) configuration expressed as gain (top) and phase (bottom) ratio over frequency. Mean response value and 2σ error bars obtained using the LPM^{47,49} across three (#47080, #47086, #47118), four (#47083, #47116) and 13 periods (#47119). The fitted model represents a deliberate worst-case fit⁴⁶, aimed at guaranteeing stability margins when used to design a feedback controller.

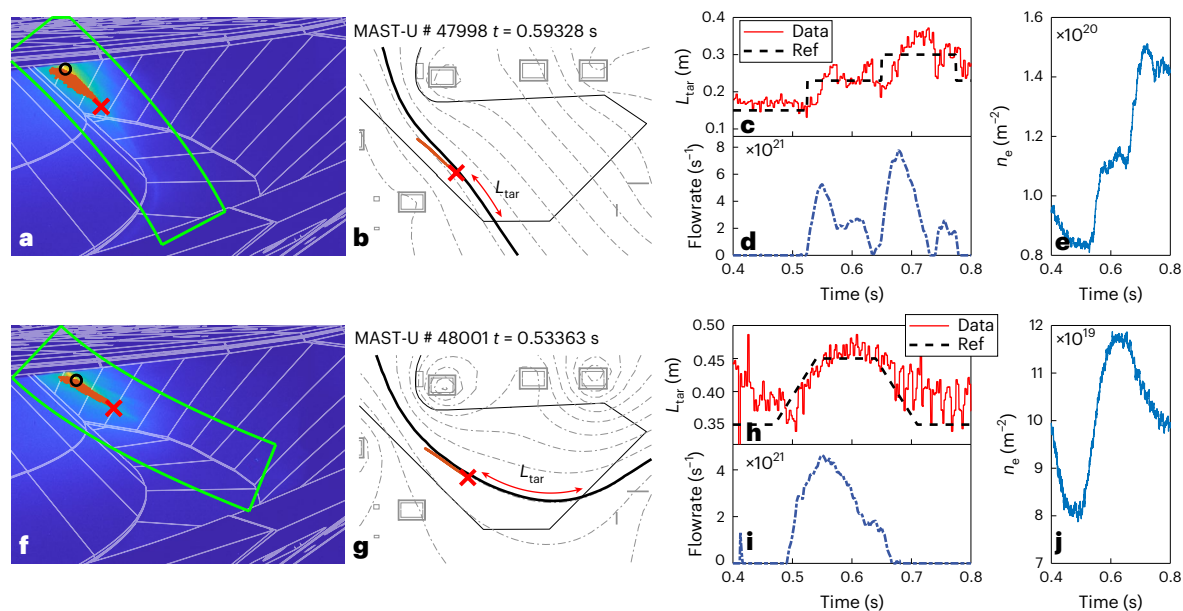


Fig. 5 | Feedback exhaust control in Elongated and Super-X divertor configuration in MAST-U. **a–j**, The Elongated divertor in experiment number 47998 (**a–e**) and the Super-X divertor in experiment number 48001 (**f–j**). **a, f**, Fulcher-band-filtered MWI⁴⁴ image with 3D model wireframe overlay (white lines). The green box indicates the region where the emissions front-tracking algorithm⁵¹ is active; the divertor leg pixels (orange dots) are detected through a 50% threshold on the maximum intensity (black circle) with the front position

(red cross) taken as the divertor pixel nearest to the target. **b, g**, Front-tracking result transformed to the poloidal cross-section with the Equilibrium Fitting (EFIT++) magnetic equilibrium reconstruction (black) overlay, including flux contour lines (dashed). **c, h**, Time evolution of the poloidal distance-to-target L_{tar} and its applied reference. **d, i**, Time evolution of the D_2 gas flow rate request by the controller. **e, j**, Time evolution of core line-integrated electron density.

bandwidth of 9.5 Hz and high 70° phase margin⁵⁰, indicating that future performance improvements are probably possible.

Feedback detachment control requires real-time inference of the ionization front position. An inversion-less tracking algorithm⁵¹, directly operating on raw camera images, is adopted for this real-time implementation. Although yielding comparable results to the inverted technique, its coordinate transformation^{51,52} introduces additional noise and limitations (Extended Data Fig. 7, Methods).

Detachment control is successfully achieved using the same controller for both ED and SXD (Fig. 5): in both scenarios, the controller adeptly follows the reference trajectory. This illustrates the robustness of our detachment control implementation; the same approach is successful for two distinct divertor configurations. In contrast, achieving detachment control in CD configuration, for this specific scenario and fuelling location, would be virtually impossible as the front quickly moves from near the strikepoint to outside the divertor chamber and remains there. This happens within the 2.5-ms acquisition time of the MWI (Extended Data Fig. 3), too fast for the gas system to act upon.

When the controller aims to move the front towards the target, the gas flow is reduced, however the ionization front moves slower than requested (Fig. 5f–j). This is probably due to the high divertor neutral pressure given the present lack of cryopumping⁴⁰ in MAST-U, illustrating the importance of adequate pumping for exhaust control, consistent with the impurity retention issues noted in TCV²⁵.

We have demonstrated exhaust control in ADCs. Crucially, this now proves their compatibility with exhaust control as required for (compact) fusion power reactors. A key requirement for double-null power reactor designs is independent exhaust control of the lower/upper divertors to combat the expected asymmetric transients from divertor power-sharing imbalances^{8,10}. Therefore, we investigate the coupling between the upper and lower divertors in the next section.

Upper–lower divertor coupling

Thus far, open divertor geometries have exhibited a clear coupling between upper and lower divertors³³. Here we systematically investigate

this coupling for the strongly baffled divertor chambers in MAST-U, demonstrating the key benefits of ADCs for enabling independent control of the divertor regions.

As opposed to perturbing core fuelling, individual system identification perturbations using upper and lower divertor gas valves are performed. When perturbing only the lower divertor D_2 gas valve, a clear response is observed in both the lower divertor ionization front position L_{tar} and lower divertor D_{alpha} filterscope (Fig. 6). Conversely, the upper D_{alpha} filterscope indicates no response to this perturbation (Extended Data Fig. 6).

Subsequently, only the upper divertor valve is perturbed (Fig. 7). Whereas we observe a clear response in the upper D_{alpha} filterscope intensity, no response in the lower divertor ionization front position nor D_{alpha} intensity is observed. Additionally, the lower divertor is substantially less deeply detached than during the lower divertor perturbation (Fig. 6). This disparity suggests a limited influence of the upper divertor perturbation on the lower divertor state, demonstrating a clear decoupling between the two divertors. This is a major result, confirming preliminary, static observations¹⁴.

Preliminary He seeding experiments have indicated that He injected in the lower divertor does spread rapidly to the core and upper divertor, potentially limiting the observed decoupling to neutral pressure only, prompting further study. We attribute the observed decoupling for D_2 to the strong neutral baffling of the divertor chamber as such decoupling is absent in open divertor geometries⁵³.

Our findings prove that instabilities driven by interaction between the upper and lower divertor controllers are highly unlikely using D_2 actuation. The required independent control of both divertor regions can therefore likely be achieved, crucial for ADC deployment in fusion power reactors.

Discussion

In this work, we have demonstrated key benefits of ADCs for exhaust control: (1) a highly reduced sensitivity to perturbations that enables active exhaust control in otherwise unfeasible situations and facilitates (2) a

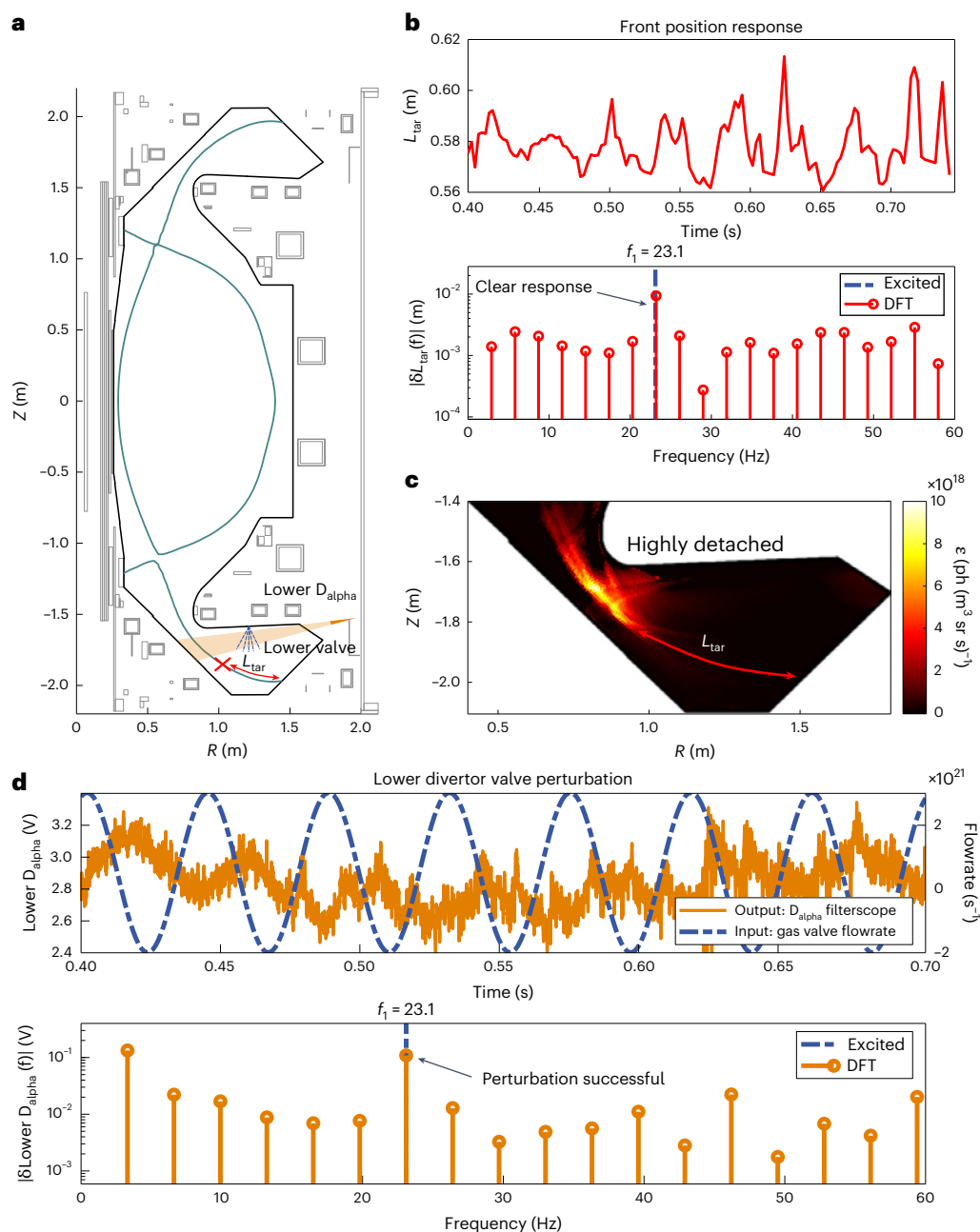


Fig. 6 | Lower divertor gas valve system identification in Super-X divertor configuration. **a**, Poloidal cross-section showing the EFIT++ magnetic equilibrium reconstruction ($t = 0.55$ s) with a conceptual illustration of the lower divertor D_{α} filterscope sightline, lower divertor valve location and lower divertor Fulcher band front position L_{tar} . **b**, Time domain (top) and frequency domain (bottom) response of the detrended lower divertor Fulcher band

front position L_{tar} around the operating point. **c**, MWI Fulcher band inversion ($t = 0.55$ s), indicating highly detached conditions. **d**, Time domain (top) and frequency domain (bottom) response of the detrended lower divertor D_{α} filterscope (-) around the operating point to a perturbation of the requested lower D_2 divertor gas valve flow rate (-). All data from experiment number 49297.

major increase in the ability to passively absorb fast transients, which would otherwise damage the divertor; furthermore, (3) a strong isolation of each divertor from other reactor regions enables near-independent control of the divertors and core plasma. These benefits illustrate how ADCs are extremely beneficial for exhaust control, forming a viable risk-mitigation strategy for power exhaust handling in fusion reactors.

A practical application of ADCs is STEP, targeting completion in the 2040s and ultimately aiming to deliver power to the UK grid⁷⁻¹⁰. The compact reactor features tightly baffled long-legged divertors, with an increased strikepoint radius in a double-null configuration (Fig. 8a and Extended Data Fig. 8), strongly resembling the MAST-U set-up.

Beyond illustrating the capabilities of ADCs to mitigate key risks in reactors, our research also has practical implications for reactor detachment control. Monitoring the detached regime is generally complex, requiring detailed analysis techniques that are challenging to be applied in real time^{14,15,54}. This work enables real-time detachment diagnosis, using D_2 Fulcher band emissions as a direct indicator for the detachment front location.

We demonstrate the scientific feasibility of this sensor technique by post-processing³⁹ STEP SOLPS-ITER simulations¹⁰ to generate D_2 Fulcher emissions profiles and subsequently produce synthetic brightness signals (Fig. 8d). As opposed to using imaging systems,

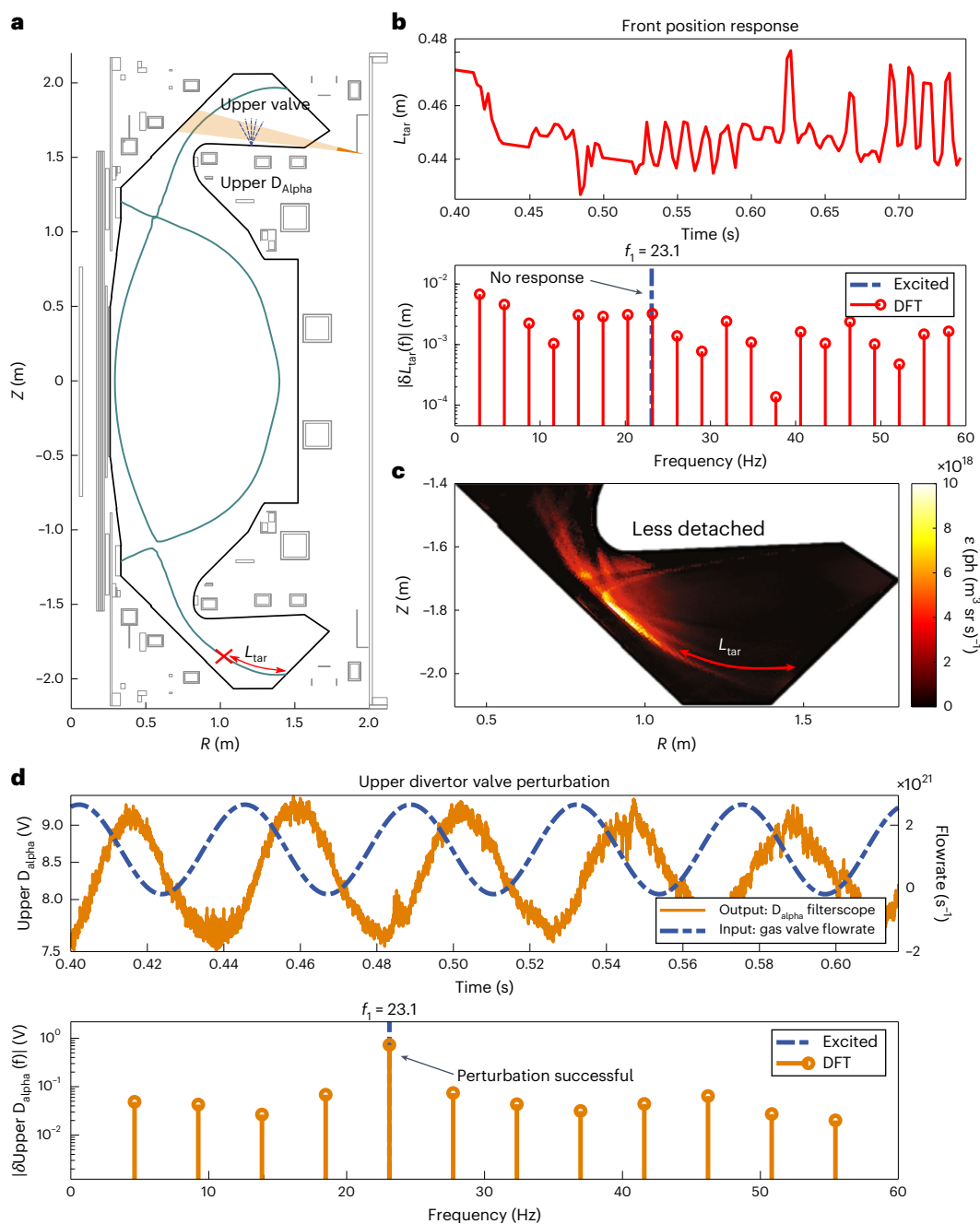


Fig. 7 | Upper divertor gas valve system identification in Super-X divertor configuration. **a**, Poloidal cross-section showing the EFIT++ magnetic equilibrium reconstruction ($t = 0.55$ s) with a conceptual illustration of the upper divertor D_{α} filterscope sightline, upper divertor valve location and lower divertor Fulcher band front position L_{tar} . **b**, Time domain (top) and frequency domain (bottom) response of the detrended lower divertor Fulcher band

front position L_{tar} around the operating point. **c**, MWI Fulcher band inversion ($t = 0.55$ s), indicating highly detached conditions. **d**, Time domain (top) and frequency domain (bottom) response of the detrended upper divertor D_{α} filterscope (-) around the operating point to a perturbation of the requested upper D_2 divertor gas valve flow rate (-). All data from experiment number 49298.

our sensor technique can even work with this synthetic spectroscopy set-up with a limited, fictitious, viewing geometry (Fig. 8b). Such an implementation can be shielded from the harsh reactor environment⁵⁵ and is thus more reactor relevant. The simulation shows a highly detached lower divertor as a result of a power-sharing imbalance, originating from an upward shift in the plasma equilibrium towards an upper single null¹⁰. With most power flowing to the upper divertor, the lower divertor ionization front moves upstream (Fig. 8c). Such power-sharing imbalances are a key challenge in STEP^{8,10}, our results show how this can be diagnosed by tracking the D_2 Fulcher emissions

profile in the lower divertor, demonstrating the scientific feasibility of the highlighted sensor technique in reactors. Consequently, it is well suited to play a central role in the diagnostic set, which includes measurements targeting the *attached* regime, to fully diagnose the divertor for exhaust control.

The ultimate goal of an exhaust control system is to maintain acceptable exhaust conditions in the presence of disturbances, requiring: (1) divertor diagnosis, (2) passive transient absorption and (3) independent control of both divertors. Our pioneering MAST-U results show great promise in these aspects. Independent, simultaneous control of

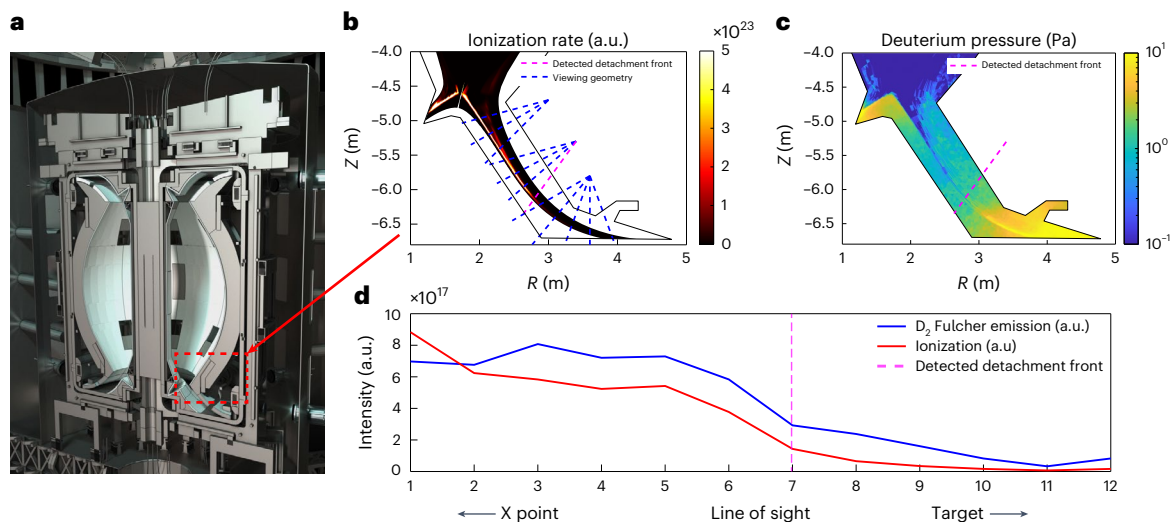


Fig. 8 | Conceptual STEP divertor detachment sensor. a, Artistic impression of the STEP reactor^{7–10}, with the lower divertor region indicated by the red box. **b**, Divertor ionization rate in an early design of STEP for a deeply detached Scrape-Off Layer Plasma Simulation (SOLPS)-ITER¹⁰ with overlaid synthetic spectroscopy viewing geometry and detected detachment front. **c**, Divertor D_2

pressure, with overlaid detected detachment front. **d**, Synthetic D_2 Fulcher band spectroscopy signals, using Fulcher emissions profiles generated by post-processing³⁹, for the sightlines shown in **b**, indicating the correlation to the ‘true’ ionization source from the simulation and subsequent detection of the detachment front. a.u., arbitrary units. Credit: **a**, UK Industrial Fusion Solutions.

the lower/upper divertors is a major milestone planned to be demonstrated in the 2024–2025 MAST-U physics campaign. Higher external heating levels (>10 MW) are planned from 2026, enabling experimental validation at more reactor-relevant powers and studies employing a blend of hydrogenic and impurity gasses as required for power exhaust control in reactors^{8,24}.

To conclude, we have demonstrated that alternative divertors are compatible with exhaust control, as required for fusion power reactors. We highlighted major benefits for exhaust control, confirming alternative divertors as a viable risk-mitigation strategy towards manageable heat loads in (compact) fusion reactors.

Methods

MAST-U fusion experiment

The Mega Ampere Spherical Tokamak Upgrade (MAST-U) is a tokamak fusion research experiment operated by the United Kingdom Atomic Energy Authority at Culham Campus^{40,41} (Extended Data Fig. 1). It is a compact, spherical¹¹ device with a major radius of 0.85 m and minor radius of 0.65 m, featuring a double-null design, that is, it has both upper and lower divertors. MAST-U is especially constructed to explore various alternative divertor configurations through its extreme divertor shaping capabilities in the large divertor chamber. This notably includes the Super-X alternative divertor configuration^{38,39,56}. Both divertor chambers are closed off from the main chamber (that is, strongly baffled⁴²) to increase neutral compression, further improving exhaust performance⁴¹.

Experimental scenario

The experiments in this work were executed in the second and third MAST-U operating campaigns. We employ a plasma current of 750 kA and we use 1.5-MW South-West Neutral Beam Injection to increase core temperature, leading to increased power flowing into the divertor region. Low-confinement (L-mode) operation was selected over High-confinement (H-mode), as the available H-mode scenario is often more deeply detached compared to L-mode. This causes the ionization front to be out of view of the MWI diagnostic. A build-up of divertor chamber neutral pressure was generally observed in these experiments. The commissioning of the MAST-U cryopumps in the upcoming campaign will probably aid in avoiding this.

A D_2 main chamber gas valve located on the low-field side is used for plasma fuelling perturbations, in addition, perturbations were applied with upper and lower divertor valves for some experiments. Density control⁴⁶ is employed to achieve line-averaged densities of $2\text{--}3 \times 10^{19} \text{ m}^{-3}$ before it is disabled during the perturbation or feedback-control phase of the experiments. In addition to the Conventional divertor, we employ the Elongated and Super-X alternative divertor configurations in this study.

Alternative divertor configurations

Alternative divertor configurations (ADCs) are considered as an exhaust solution for future devices through their superior performance with respect to conventional divertors, with several different designs currently under investigation^{16,37,57}. These designs leverage variations in magnetic topology to enhance particle, power and momentum losses in the divertor region and spread the power over a larger area. This leads to a lower plasma temperature, heat flux and, in some cases, increased access to the detached plasma regime^{14–16}. Drawbacks of alternative designs however are engineering complexity (especially in magnetic coil design) and a spatially larger divertor within the vacuum vessel^{34,37}. This leads to increased costs for ADCs in comparison to conventional divertors. Hence, any reactor featuring ADCs has to strike the balance between these drawbacks and the improved performance ADCs offer. ADCs can therefore serve as a risk-mitigation strategy for when conventional divertors cannot withstand the power exhaust in a reactor implementation.

One of the most prominent ADCs, and the focus of this work, is the Super-X divertor^{38,39,56} (Fig. 1). In this configuration, the total flux expansion (F_R) is maximized, that is, maximizing the cross-section area of a flux tube¹⁷. For the conventional divertor considered in this paper $F_R \approx 1.2$, whereas $F_R \approx 2.3$ for the Super-X configuration¹⁶. To achieve this, the strikepoint is placed at large major radius¹⁷ as $F_R \propto 1/B$. This also leads to an increased surface area on which the power is deposited and promotes interaction with neutral particles through an increased particle path of travel (connection length) from X point to target. The Super-X design has demonstrated to substantially improve the target conditions, facilitate an increased access to the detached plasma regime^{14–16} and, in this paper, substantial benefits in handling fast transients.

We also consider the Elongated divertor configuration in this work (Fig. 1). This design only employs moderate total flux expansion

($F_R \approx 1.7$) compared to the Super-X but has been demonstrated to already achieve substantial performance gains^{14–16}.

MAST-U gas system

The MAST-U gas system consists of a collection of piezo-electric gas valves, which connect to the vacuum vessel through pipes, with various injection points in both main chamber and divertor⁵⁸. Calibrations are used to convert a requested gas flow rate to a voltage, which is subsequently applied to the piezo element. These calibrations are static and hence do not take any gas valve or gas flow dynamics into account. In addition, they assume a linear voltage-to-flow rate relation, which is not accurate near the closing voltage⁵⁹ and does not take hysteresis of the piezo element into account. The injected gas flow rate, therefore, carries considerable uncertainty⁴⁶ and is occasionally reported as negative, despite the observation of actual gas flow.

The main chamber valve used in these experiments (Fig. 1) is positioned close to a D_{α} filterscope. The D_{α} intensity measured by this diagnostic represents plasma-neutral interaction and can therefore serve as an indication of the gas system response (Extended Data Figs. 4 and 5). During the experiments presented in this paper, the utilized flow rate was quite low, operating near the gas valve closing voltage, to prevent an extremely detached divertor state where the D_2 Fulcher band is out of view of the MWI diagnostic (Fig. 1). Therefore, we can observe some distortion at low voltages, evident as nonlinear components in the frequency domain⁴⁹. The high signal-to-noise ratio of this D_{α} filterscope measurement allows for a low average noise level, hence, these nonlinear components can be observed.

D_{α} filterscopes positioned in the upper (Fig. 7) and lower (Fig. 6) divertors are employed to also check the functioning of the respective divertor valves. These signals carry more noise compared to the main chamber signals because the divertor filterscopes are toroidally positioned further away from their valves, nevertheless, they clearly show the divertor valve perturbations (Figs. 6 and 7).

D_2 Fulcher band emissions

Throughout this work, we use D_2 Fulcher band emissions to diagnose the divertor conditions. D_2 Fulcher band emissions originate from electronically excited molecules after electron-impact collisions. Strong Fulcher band emissions occurs at 4–5 eV, similar to atomic ionization. Therefore, Fulcher band emissions have been presented as a quantitative method to infer the hydrogen ionization front position^{14,60}. The steep temperature dependence of D_2 electronic excitation creates a clearly defined front position, that is, the position of the downstream end of the ionization bulk. This front position can be tracked relatively easily using filtered imaging or spectroscopy. The position of this ionization region is a fundamental indicator of the divertor detachment state^{14,15,54}. Contrary to impurity emissions fronts, which are routinely used to diagnose detachment^{19,25,53}, Fulcher band emissions are unaffected by impurity transport. This results in a more reliable, machine-independent and direct indication of the divertor detachment state.

Inversion-based front tracking

Tracking of the Fulcher band emissions front is achieved using spectrally filtered images from the Multi-Wavelength-Imaging camera system^{44,61}, positioned in the lower divertor of MAST-U (Figs. 1a and 5a,f). The raw camera images from the Fulcher band-filtered channel (Fig. 5a,f) are inverted to obtain a poloidal emissivity profile (Figs. 6c and 7c). The front position is then taken as the position with 50% extinction from the maximum intensity⁴⁵. The front tracking algorithm outputs L_{tar} and L_x , the distance from the emissions front to the divertor target and X point, measured along the divertor leg in the poloidal plane (Fig. 3d).

The Conventional divertor leg is largely out of view of the MWI diagnostic. Therefore, we employ the newly available X-point Imaging System (XPI) to achieve front tracking for the Conventional divertor in a

similar manner. This system was not yet available in the earlier Super-X and Elongated divertor midplane fuelled system identification and feedback-control experiments. Combined XPI and MWI inversions are performed for the tracking of the divertor fuelled system identification experiments (Figs. 6 and 7c).

The MWI, XPI or combined inversions required for this front-tracking method are computationally expensive, hence, front tracking using inverted images is currently only available offline, that is, after the experiment has completed⁴⁵. Machine-learning-based acceleration techniques have shown promising results⁶² and might allow for a future extension to real-time operation. In this paper, we employ inversion-based front tracking only for offline analysis of system identification experiments, and we rely on a different routine for real-time front tracking.

Real-time front tracking

Real-time emissions front tracking is achieved using raw, un-inverted camera images directly through a dedicated algorithm first employed in the TCV tokamak⁵¹. A dedicated fast coordinate transformation⁵² is used to achieve the transform from raw camera images to the poloidal plane without requiring camera inversion. Although real-time capable, the coordinate transformation introduces additional noise. We take the front as the 50% extinction from the maximum intensity along the leg, identical to the inversion-based front tracking routine (Fig. 5a,f). In absence of a real-time magnetic equilibrium reconstruction, we prescribe the divertor leg position a priori such that the distance to target along the divertor leg L_{tar} can be calculated (Fig. 5b,g). The full front tracking algorithm is executed within the 2.5-ms acquisition and processing window of the MWI diagnostic, allowing for 400-Hz operation. The computed front position is fed through an optical-analogue connection into the plasma control system⁵⁸ where the exhaust controller is located.

The divertor baffle obscures the upper part of the leg (Fig. 2). As the front is defined as an intensity threshold relative to the maximum intensity, tracking is only reliable while the maximum intensity point is in view. The divertor is consistently deeply detached in our experiments and hence, the front is located close to the divertor entrance, but still mostly remains in view (Fig. 5a,f). Tests with a fixed emission threshold (requiring careful tuning) have not shown a notable difference compared to the standard algorithm using a variable threshold. Hence, the obstruction by the divertor baffle has not substantially impacted these experiments.

The use of the fast coordinate transformation⁵² introduces a requirement for tangential sightlines. A camera system records a two-dimensional projection of a three-dimensional feature, implying that each individual pixel in the camera image records the line-integrated emissions along its sightline. Pixels corresponding to a sightline that is tangent to the light-emitting divertor leg will show a peak in intensity compared to neighbouring sightlines that either intersect or miss the leg⁵². Therefore, only the sightlines that are tangential to the divertor emissions result in a recognizable divertor leg on the raw camera image, potentially restricting the observable range to only part of the divertor leg.

We analyse the observable region for real-time front tracking through a dedicated geometric analysis and synthetic camera images; Extended Data Fig. 7. We consider both the Elongated (Extended Data Fig. 7a–e) and Super-X (Extended Data Fig. 7f–j) divertor geometries used in the experiments presented in this work and a purely synthetic Super-X divertor variant (Extended Data Fig. 7k–o) for illustrative purposes only. The camera positions, viewing geometry and synthetic camera images are inferred from spatial calibrations obtained through the CALCAM⁶³ software package. The core assumption of this analysis is that the divertor emission is located on the magnetic divertor leg. The sightlines, which are blocked by the divertor tiles, are shown in red whereas the observable sightlines are shown in green (Extended Data

Fig. 7a,b,f,g,k,l). In the poloidal plane, a negative dR/dZ is required for a tangential point to exist, otherwise, a sightline will intersect with the plasma by definition. We designate the point where dR/dZ changes sign as the inflection point. Note that although a tangential point might exist, it can still be outside the camera view or be obstructed by the divertor tiles. Such cases have been treated as if no sightline exists. In Elongated geometry, the full leg can be observed from divertor baffle to target. However, for the Super-X divertor geometries, no tangential sightline exists near the target. The location of the inflection point greatly influences the observable region near the target, evident by comparing the two Super-X geometry variants (Extended Data Fig. 7). This is supported by synthetic camera images (Extended Data Fig. 7e,j,o), generated using poloidal emissions profiles with constant emissions intensity along the entire divertor leg (Extended Data Fig. 7e,j,o). The synthetic camera images illustrate how the divertor leg is not observable after the inflection point as determined by the geometric analysis. We therefore conclude that the observable region for emissions front tracking in MAST-U using raw camera images from the MWI diagnostic is bound by the baffle at the divertor entrance and the inflection point near the divertor target.

In the experiments presented in this work, the Super-X divertor is always in a detached state, that is, the Fulcher band emission is far removed from the target. Furthermore, the Super-X geometry features an inflection point location close to the target (Extended Data Fig. 7h). We therefore conclude that the lower limit for real-time front tracking has not influenced these experiments. Nevertheless, the real-time front tracking range can be severely limited for other Super-X divertor geometries (for example, Extended Data Fig. 7m), especially in more attached conditions. The inflection point location should therefore be taken into account when selecting a divertor geometry for feedback exhaust control experiments. Note that these restrictions only apply to the real-time front tracking required for feedback control; the offline inversion-based front tracking method is unaffected.

System identification

We experimentally identify the exhaust dynamics in MAST-U through system identification. This method relies on observing the system response to applied perturbations and has been employed successfully to identify the exhaust dynamics on several devices^{19,25,64}. In addition to allowing for the *design* of a feedback controller, the experimental identification of exhaust dynamics supports the development of physics-based dynamic models to inform control system design for future devices.

The considered dynamic system (Fig. 1b) includes the gas system, plasma response and MWI sensor dynamics. Note that the dynamics of the piezo-electric gas valve and its associated piping is included in the system (MAST-U gas system section). The system input is the requested flow rate u , the output is the Fulcher band poloidal emission front position L_{tar} .

We perturb the system input with especially designed signals, consisting of a single sine or a sum of sinusoidal signals. This allows the signal power to be focussed on specific frequencies of interest. We use only a few frequencies per experiment, driven by the low signal-to-noise ratios generally observed in detachment measurements¹⁹. The available time for perturbation is only 300–400 ms due to the relatively short <1 s total experiment duration in MAST-U. We require at least three periods per frequency to generate error bars on the data, the lowest frequency within the measurement window is therefore around 8–10 Hz. The upper limit is set by the gas system; above this limit, the gas system will no longer follow the prescribed perturbation signal, taken as roughly 50 Hz (ref. 64).

The perturbation signals consist of integer multiples, or harmonics (f_3, f_5, f_{\dots}), of the ground frequency (f_1). The ground frequency is determined as the lowest frequency which completes three periods within the measurement window and matches the sampling rates of all considered diagnostics and actuators to prevent aliasing. Generally,

only odd frequency components are excited to observe possible quadratic nonlinear effects^{47,49}. However, this quickly drives us towards frequencies above the stipulated 50-Hz gas system limit. Therefore, we occasionally opt to use f_1 and f_2 or perturb only a single frequency per experiment.

The input and output signals are transformed from the time domain to the frequency domain using the discrete Fourier transform; Extended Data Fig. 2. We estimate an average noise level by taking the average response on the non-excited frequencies, excluding frequencies lower than f_1 to remove transient effects^{49,65}. The discrete-Fourier-transform response contains predominantly only excited frequencies well above the average noise level for the considered frequency range, indicating dominantly linear dynamics⁴⁹. Occasionally, some harmonics do exceed the average noise level (most apparent in Extended Data Fig. 2a). As these nonlinear components are already apparent in the D_{alpha} filterscope measurement (Extended Data Fig. 4), they originate from the gas system and not the plasma dynamics themselves.

We identify the Frequency Response Function (FRF) of the system by dividing the observed output over input in frequency domain. The Local Polynomial Method is used^{47,49} to correct for transient effects. The FRF is a local linearization of the input–output dynamics; nonlinear effects will not be captured by the FRF. This is standard practice in control theory and applicable for this predominantly linear system.

STEP fusion power reactor

The Spherical Tokamak For Energy Production (STEP) is a tokamak currently in the concept design phase (Extended Data Fig. 8). It is a highly ambitious programme, targeting completion in the 2040s with the ultimate aim of demonstrating the delivery of fusion power to the UK grid^{7–10}. The initial design considered in this paper has a major radius of 3.6 m and should deliver 120 MW electrical power. STEP is a spherical tokamak, equipped with two tightly baffled⁴² divertor chambers which facilitate long-legged divertor configurations, akin to MAST-U (Extended Data Fig. 1). Although it shares a similar design philosophy to MAST-U, its design is fundamentally differently in coping with the neutral irradiation, power cycle, tritium fuel cycle and other requirements placed on a fusion power reactor. Unlike the large divertor volume in MAST-U for facilitating the SXD, the STEP design is less extreme, in some ways resembling the MAST-U ED configuration. The requirement of an exhaust control system for STEP to ensure manageable heat loads is a core driver for the work presented in this paper.

The STEP SOLPS-ITER simulations considered in this work have been published previously as part of a power-sharing study featuring an early design iteration¹⁰. The specific simulation considered features a highly detached lower divertor (Fig. 8) through an upward shift in the plasma equilibrium towards an upper single null. This causes the bulk of the power to flow to the upper divertors, leading to a highly detached lower divertor state.

Data availability

The data that support these studies are available at <https://doi.org/10.14468/7fj-p470>. Source data are provided with this paper.

Code availability

The code used to generate the figures and analyse the data was developed by the authors and is available via Zenodo at <https://doi.org/10.5281/zenodo.13830756> (ref. 66).

References

1. Cowley, S. C. The quest for fusion power. *Nat. Phys.* **12**, 384–386 (2016).
2. Wesson, J. *Tokamaks* (Oxford Univ. Press, 2004).
3. Pitts, R. A. et al. Physics basis for the first ITER tungsten divertor. *Nucl. Mater. Energy* **20**, 100696 (2019).

4. Zohm, H. et al. The EU strategy for solving the DEMO exhaust problem. *Fusion Eng. Des.* **166**, 112307 (2021).
5. Sorbom, B. et al. ARC: a compact, high-field, fusion nuclear science facility and demonstration power plant with demountable magnets. *Fusion Eng. Des.* **100**, 378–405 (2015).
6. Creely, A. J. et al. Overview of the SPARC tokamak. *J. Plasma Phys.* **86**, 865860502 (2020).
7. Baker, A. The Spherical Tokamak for Energy Production (STEP) in context: UK public sector approach to fusion energy. *Philos. Trans. R. Soc. A* **382**, 20230401 (2024).
8. Lennholm, M. et al. Controlling a new plasma regime. *Philos. Trans. R. Soc. A* **382**, 20230403 (2024).
9. Henderson, S. et al. An overview of the STEP divertor design and the simple models driving the plasma exhaust scenario. *Nucl. Fusion* **65**, 016033 (2025).
10. Osawa, R. et al. SOLPS-ITER analysis of a proposed STEP double null geometry: impact of the degree of disconnection on power-sharing. *Nucl. Fusion* **63**, 076032 (2023).
11. Peng, Y.-K. M. et al. Spherical torus - an approach to compact fusion at low field: initial ignition assessments. *Fusion Technol.* **8**, 338 (1985).
12. Hudoba, A., Newton, S., Voss, G., Cunningham, G. & Henderson, S. Divertor optimisation and power handling in spherical tokamak reactors. *Nucl. Mater. Energy* **35**, 101410 (2023).
13. Kuang, A. Q. et al. Divertor heat flux challenge and mitigation in SPARC. *J. Plasma Phys.* **86**, 865860505 (2020).
14. Verhaegh, K. et al. The role of plasma-atom and molecule interactions on power & particle balance during detachment on the MAST upgrade Super-X divertor. *Nucl. Fusion* **63**, 126023 (2023).
15. Verhaegh, K. et al. Investigations of atomic and molecular processes of NBI-heated discharges in the MAST upgrade Super-X divertor with implications for reactors. *Nucl. Fusion* **64**, 086050 (2024).
16. Verhaegh, K. et al. Divertor shaping with neutral baffling as a solution to the tokamak power exhaust challenge. *Commun. Phys.* **8**, 215 (2025).
17. Theiler, C. et al. Results from recent detachment experiments in alternative divertor configurations on TCv. *Nucl. Fusion* **57**, 072008 (2017).
18. Loarte, A. & Neu, R. Power exhaust in tokamaks and scenario integration issues. *Fusion Eng. Design* **122**, 256–273 (2017).
19. Ravensbergen, T. et al. Real-time feedback control of the impurity emission front in tokamak divertor plasmas. *Nat. Commun.* **12**, 1105 (2021).
20. Wiesen, S. et al. Control of particle and power exhaust in pellet fuelled ITER DT scenarios employing integrated models. *Nucl. Fusion* **57**, 076020 (2017).
21. De Temmerman, G., Kirk, A., Nardon, E., Tamain, P. & The MAST Team. Heat load asymmetries in MAST. *J. Nucl. Mater.* **415**, S383–S386 (2011).
22. Morgan, T., Li, Y., Balden, M., Brezinsek, S. & De Temmerman, G. Combined high fluence and high cycle number transient loading of ITER-like monoblocks in Magnum-PSI. *Nucl. Fusion* **61**, 116045 (2021).
23. Lipschultz, B., Parra, F. I. & Hutchinson, I. H. Sensitivity of detachment extent to magnetic configuration and external parameters. *Nucl. Fusion* **56**, 056007 (2016).
24. Biel, W. et al. Development of a concept and basis for the DEMO diagnostic and control system. *Fusion Eng. Design* **179**, 113122 (2022).
25. Koenders, J. et al. Model-based impurity emission front control using deuterium fueling and nitrogen seeding in TCv. *Nucl. Fusion* **63**, 026006 (2023).
26. Kallenbach, A. et al. Partial detachment of high power discharges in ASDEX Upgrade. *Nucl. Fusion* **55**, 053026 (2015).
27. Eldon, D. et al. Advances in radiated power control at DIII-D. *Nucl. Mater. Energy* **18**, 285–290 (2019).
28. Bernert, M. et al. X-point radiation, its control and an ELM suppressed radiating regime at the ASDEX upgrade tokamak. *Nucl. Fusion* **61**, 024001 (2021).
29. Xu, G. S. et al. Divertor impurity seeding with a new feedback control scheme for maintaining good core confinement in grassy-ELM H-mode regime with tungsten monoblock divertor in EAST. *Nucl. Fusion* **60**, 086001 (2020).
30. Brunner, D. et al. Feedback system for divertor impurity seeding based on real-time measurements of surface heat flux in the Alcator C-Mod tokamak. *Rev. Sci. Instrum.* **87**, 023504 (2016).
31. Kolemen, E. et al. Heat flux management via advanced magnetic divertor configurations and divertor detachment. *J. Nucl. Mater.* **463**, 1186–1190 (2015).
32. Guillemaut, C. et al. Real-time control of divertor detachment in H-mode with impurity seeding using Langmuir probe feedback in JET-ITER-like wall. *Plasma Phys. Controlled Fusion* **59**, 045001 (2017).
33. Kallenbach, A. et al. Optimized tokamak power exhaust with double radiative feedback in ASDEX upgrade. *Nucl. Fusion* **52**, 122003 (2012).
34. Reimerdes, H. et al. Assessment of alternative divertor configurations as an exhaust solution for DEMO. *Nucl. Fusion* **60**, 066030 (2020).
35. van Eden, G. G., Kvon, V., van de Sanden, M. C. M. & Morgan, T. W. Oscillatory vapour shielding of liquid metal walls in nuclear fusion devices. *Nat. Commun.* **8**, 192 (2017).
36. Bernert, M. et al. The X-Point radiating regime at ASDEX Upgrade and TCv. *Nucl. Mater. Energy* **34**, 101376 (2023).
37. Militello, F. et al. Preliminary analysis of alternative divertors for DEMO. *Nucl. Mater. Energy* **26**, 100908 (2021).
38. Havlíčková, E. et al. SOLPS analysis of the MAST-U divertor with the effect of heating power and pumping on the access to detachment in the Super-x configuration. *Plasma Phys. Control. Fusion* **57**, 115001 (2015).
39. Moulton, D. et al. Super-X and conventional divertor configurations in MAST-U ohmic L-mode; a comparison facilitated by interpretative modelling. *Nucl. Fusion* **64**, 076049 (2024).
40. Morris, W. et al. MAST upgrade divertor facility: a test bed for novel divertor solutions. *IEEE Trans. Plasma Sci.* **46**, 1217–1226 (2018).
41. Fishpool, G. et al. MAST-upgrade divertor facility and assessing performance of long-legged divertors. *J. Nucl. Mater.* **438**, S356–S359 (2013).
42. Reimerdes, H. et al. Initial TCv operation with a baffled divertor. *Nucl. Fusion* **61**, 024002 (2021).
43. Wigram, M. et al. Performance assessment of long-legged tightly-baffled divertor geometries in the ARC reactor concept. *Nucl. Fusion* **59**, 106052 (2019).
44. Feng, X. et al. Development of an 11-channel multi wavelength imaging diagnostic for divertor plasmas in MAST upgrade. *Rev. Sci. Instrum.* **92**, 063510 (2021).
45. Wijkamp, T. et al. Characterisation of detachment in the MAST-U Super-X divertor using multi-wavelength imaging of 2D atomic and molecular emission processes. *Nucl. Fusion* **63**, 056003 (2023).
46. Derks, G. et al. Development of real-time density feedback control on MAST-U in L-mode. *Fusion Eng. Des.* **202**, 114387 (2024).
47. Van Berkel, M. et al. Correcting for non-periodic behaviour in perturbative experiments: application to heat pulse propagation and modulated gas-puff experiments. *Plasma Phys. Controlled Fusion* **62**, 094001 (2020).

48. Lipschultz, B. et al. Marfe: an edge plasma phenomenon. *Nucl. Fusion* **24**, 977–988 (1984).
49. Schoukens, J., Vandersteen, G., Barbé, K. & Pintelon, R. Nonparametric preprocessing in system identification: a powerful tool. *Eur. J. Control* **15**, 260–274 (2009).
50. Skogestad, S. & Postlethwaite, I. *Multivariable Feedback Control: Analysis and Design* (John Wiley; Sons, 2005).
51. Ravensbergen, T. et al. Development of a real-time algorithm for detection of the divertor detachment radiation front using multi-spectral imaging. *Nucl. Fusion* **60**, 066017 (2020).
52. Hommen, G. *Optical Boundary Reconstruction for Shape Control of Tokamak Plasmas*. PhD thesis, Technische Universiteit Eindhoven (2014); <https://pure.tue.nl/ws/portalfiles/portal/4029763/780045.pdf>
53. Février, O. et al. Detachment in conventional and advanced double-null plasmas in TCV. *Nucl. Fusion* **61**, 116064 (2021).
54. Perek, A. et al. A spectroscopic inference and SOLPS-ITER comparison of flux-resolved edge plasma parameters in detachment experiments on TCV. *Nucl. Fusion* **62**, 096012 (2022).
55. Luís, R. et al. Nuclear analysis of the DEMO divertor survey visible high-resolution spectrometer. *Fusion Eng. Des.* **169**, 112460 (2021).
56. Valanju, P. M., Kotschenreuther, M., Mahajan, S. M. & Canik, J. Super-X divertors and high power density fusion devices. *Phys. Plasmas* **16**, 056110 (2009).
57. Labit, B. et al. Experimental studies of the snowflake divertor in TCV. *Nucl. Mater. Energy* **12**, 1015–1019 (2017).
58. McArdle, G., Pangione, L. & Kochan, M. The MAST upgrade plasma control system. *Fusion Eng. Des.* **159**, 111764 (2020).
59. Liseli, J. B., Agnus, J., Lutz, P. & Rakotondrabe, M. An overview of piezoelectric self-sensing actuation for nanopositioning applications: electrical circuits, displacement, and force estimation. *IEEE Trans. Instrum. Meas.* **69**, 2–14 (2020).
60. Osborne, N. et al. Initial Fulcher band observations from high resolution spectroscopy in the MAST-U divertor. *Plasma Phys. Control. Fusion* **66**, 025008 (2024).
61. Perek, A. et al. MANTIS: a real-time quantitative multispectral imaging system for fusion plasmas. *Rev. Sci. Instrum.* **90**, 123514 (2019).
62. Van Leeuwen, L. et al. Machine learning enhanced tomographic reconstruction for multispectral imaging on TCV. *Plasma Phys. Controlled Fusion* **67**, 025024 (2025).
63. Silburn, S. et al. CALCAM software package (version 2.5.0). Zenodo <https://doi.org/10.5281/zenodo.3956834> (2020).
64. Koenders, J. et al. Systematic extraction of a control-oriented model from perturbative experiments and SOLPS-ITER for emission front control in TCV. *Nucl. Fusion* **62**, 066025 (2022).
65. Berkel, M. V. et al. *A Model Predictive Control Strategy for the Exhaust* (ITPA DivSQL, 2023).
66. Kool, B. bob-kool/ADC_control: Final. Zenodo <https://doi.org/10.5281/zenodo.15309011> (2024).
67. Federici, F. et al. Design and implementation of a prototype infrared video bolometer (IRVB) in MAST upgrade. *Rev. Sci. Instrum.* **94**, 033502 (2023).
68. Federici, F. et al. Evolution of radiation profiles in a strongly baffled divertor on MAST Upgrade. *Nucl. Mater. Energy* **43**, 101940 (2025).

Acknowledgements

We thank C. Theiler for his foundational contributions to the development of alternative divertors under EUROfusion. We are grateful to R. Osawa for providing the SOLPS simulation of the STEP divertor. The contribution of R. Doyle in supporting operation

of the MWI diagnostic is kindly acknowledged. DIFFER is part of the institutes organization of NWO. This work has been carried out within the framework of the EUROfusion Consortium, funded by the European Union via the Euratom Research and Training Programme (grant agreement number 101052200 - EUROfusion) (B.K., K.V., G.L.D., T.A.W., J.T.W.K., N.L., G.M., C.V., S.S.H., D.B., H.R., N.O., M.B., The EUROfusion tokamak exploitation team, the MAST-U team) and from the Engineering and Physical Sciences Research Council (EPSRC) (grant numbers EP/W006839/1, EP/T012250/1, EP/N023846/1 (K.V., G.M., C.V., S.S.H., the MAST-U team) and EP/S022430/1 (N.L., N.O., F.F.)). The Swiss contribution to this work has been funded by the Swiss State Secretariat for Education, Research and Innovation (SERI) (H.R.). Views and opinions expressed are however those of the author(s) only and do not necessarily reflect those of the European Union, or the European Commission or SERI. Neither the European Union nor the European Commission nor SERI can be held responsible for them. This work was supported by the US Department of Energy under grant number DE-AC05-00OR22725 (J.L., F.F.).

Author contributions

B.K.: design, execution and analysis of the experiments; system identification analysis and interpretation of the results; exhaust controller development, implementation into the plasma control system and testing; scientific coordinator for the experiments conducted through the internal campaign; development of the front-tracking algorithm for MAST-U and its real-time implementation; main manuscript author; general coordinator of the work. K.V.: design, execution and analysis of the experiments; post-processing the provided STEP SOLPS simulation and generating synthetic spectroscopy signals; substantially contributed to writing the manuscript; discussions on the underlying physics of alternative divertor configurations. G.L.D.: design, execution and analysis of the experiments; system identification analysis and interpretation of the results; development of the core density controller employed in the experiments; development and implementation of the controller logic in the plasma control system. T.A.W.: development of camera inversion routines and real-time implementation of the front-tracking algorithm on the MWI diagnostic (main diagnostic used); involved in the experiments to ensure proper real-time operation and provided support in using the inversion routines for data analysis. J.T.W.K.: in-depth guidance during preliminary experiments, the development of the front-tracking algorithm and preparatory work in which the foundation was laid for this work. N.L.: responsible for the MWI camera system (main diagnostic used) and its operation, made necessary adjustments to the camera system and was involved in the experiments to ensure proper operation in this non-standard operating mode. G.M.: responsible for the plasma control system and conceived the real-time connection of the MWI camera system to the control system; enabled offline testing of the controller implementation in the plasma control system. C.V.: responsible for the plasma control system; ensured proper operation during experiments and enabled background testing of the controller implementation in the plasma control system. J.L.: scientific coordinator for the experiments conducted through the internal campaign; involved in the design and execution of the experiments. S.S.H.: provided support during the design of the experiments and was involved in their execution. F.F.: providing the IRVB imaging bolometer data and its inversions necessary for validating the results, assisting with its interpretation. D.B.: scientific Coordinator for the EUROfusion part of the experiments; assisted in the design and execution of the experiments. H.R.: assisted in the design of the experiments and their execution; scientific coordinator for the EUROfusion part of the experiments. N.O.: detailed analysis of the physics behind Fulcher band emissions, providing the physics basis for its use as a detachment control sensor. M.v.B.: conceptualization

of the work, guidance and substantial manuscript revisions. The EUROfusion tokamak exploitation team: funding and review of the results presented in this work. The MAST-U team: the team that is responsible for the operation of the MAST-U tokamak.

Competing interests

The authors declare no competing interests.

Additional information

Extended data is available for this paper at <https://doi.org/10.1038/s41560-025-01824-7>.

Supplementary information The online version contains supplementary material available at <https://doi.org/10.1038/s41560-025-01824-7>.

Correspondence and requests for materials should be addressed to B. Kool or K. Verhaegh.

Peer review information *Nature Energy* thanks Rui Ding and the other, anonymous, reviewer for their contribution to the peer review of this work.

Reprints and permissions information is available at www.nature.com/reprints.

Publisher's note Springer Nature remains neutral with regard to jurisdictional claims in published maps and institutional affiliations.

Open Access This article is licensed under a Creative Commons Attribution 4.0 International License, which permits use, sharing, adaptation, distribution and reproduction in any medium or format, as long as you give appropriate credit to the original author(s) and the source, provide a link to the Creative Commons licence, and indicate if changes were made. The images or other third party material in this article are included in the article's Creative Commons licence, unless indicated otherwise in a credit line to the material. If material is not included in the article's Creative Commons licence and your intended use is not permitted by statutory regulation or exceeds the permitted use, you will need to obtain permission directly from the copyright holder. To view a copy of this licence, visit <http://creativecommons.org/licenses/by/4.0/>.

© The Author(s) 2025

The EUROfusion Tokamak Exploitation Team

D. Abate⁹, J. Adamek¹⁰, M. Agostini⁹, C. Albert¹¹, F. C. P. Albert Devasagayam¹², S. Aleiferis¹³, E. Alessi¹⁴, J. Alhage¹⁵, S. Allan¹³, J. Allcock¹³, M. Alonzo¹⁶, G. Anastasiou¹⁷, E. Andersson Sunden¹⁸, C. Angioni¹⁹, Y. Anquetin²⁰, L. Appel¹³, G. M. Apruzzese¹⁶, M. Ariola²¹, C. Arnas²², J. F. Artaud²³, W. Arter¹³, O. Asztalos²⁴, L. Aucone²⁵, M. H. Aumeunier²³, F. Auremma⁹, J. Ayllon²⁶, E. Aymerich²⁷, A. Baciero²⁸, F. Bagnato⁷, L. Böhner²⁹, F. Bairaktaris¹⁷, P. Balázs²⁴, L. Balbinot⁹, I. Balboa¹³, M. Balden¹⁹, A. Balestri⁷, M. Baquero Ruiz⁷, T. Barberis³⁰, C. Barcellona³¹, O. Bardsley¹³, M. Baruzzo¹⁶, S. Benkadda²⁰, T. Bensadon³², E. Bernard²³, M. Bernert¹⁹, H. Betar³³, R. Bianchetti Morales¹³, J. Bielecki³⁴, R. Bilato¹⁹, P. Bilkova¹⁰, W. Bin¹⁴, G. Birkenmeier¹⁹, R. Bisson²², P. Blanchard⁷, A. Bleasdale¹³, V. Bobkov¹⁹, A. Boboc¹³, A. Bock¹⁹, K. Bogar¹⁰, P. Bohm¹⁰, T. Bolzonella⁹, F. Bombarda¹⁶, N. Bonanomi¹⁹, L. Boncagni¹⁶, D. Bonfiglio⁹, R. Bonifetto³⁰, M. Bonotto⁹, D. Borodin³⁵, I. Borodkina¹⁰, T. O. S. J. Bosman³⁶, C. Bourdelle²³, C. Bowman¹³, S. Brezinsek^{35,37}, D. Brida¹⁹, F. Brochard³⁸, R. Brunet²³, D. Brunetti¹³, V. Bruno²³, R. Buchholz¹¹, J. Buermans³⁹, H. Bufferand²³, P. Buratti¹⁶, A. Burckhart¹⁹, J. Cai³⁵, R. Calado⁴⁰, J. Caloud¹⁰, S. Cancelli²⁵, F. Cani⁴¹, B. Cannas²⁷, M. Cappelli¹⁶, S. Carcangiu²⁷, A. Cardinali¹⁶, S. Carli⁴², D. Carnevale⁴³, M. Carole²⁰, M. Carpita⁷, D. Carralero²⁸, F. Caruggi²⁵, I. S. Carvalho^{13,44}, I. Casiraghi¹⁴, A. Casolari¹⁰, F. J. Casson¹³, C. Castaldo¹⁶, A. Cathey¹⁹, F. Causa¹⁴, J. Cavalier¹⁰, M. Cavedon²⁵, J. Cazabonne⁷, M. Cecconello¹⁸, L. Ceelen³⁶, A. Celora²⁵, J. Cerovsky¹⁰, C. D. Challis¹³, R. Chandra¹², A. Chankin¹⁹, B. Chapman¹³, H. Chen²⁶, M. Chernyshova⁴⁵, A. G. Chiariello²¹, P. Chmielewski⁴⁵, A. Chomiczewska⁴⁵, C. Cianfarani¹⁶, G. Ciraolo²³, J. Citrin³⁶, F. Clairet²³, S. Coda⁷, R. Coelho⁴⁰, J. W. Coenen³⁵, I. H. Coffey⁴⁶, C. Colandrea⁷, L. Colas²³, S. Conroy¹⁸, C. Contre⁷, N. J. Conway¹³, L. Cordaro⁹, Y. Corre²³, D. Costa⁴⁰, S. Costea⁴⁷, D. Coster¹⁹, X. Courtois²³, C. Cowley⁴⁸, T. Craciunescu⁴⁹, G. Croci²⁵, A. M. Croitoru⁴⁹, K. Crombe³⁹, D. J. Cruz Zabala²⁶, G. Cseh²⁴, T. Czarski⁴⁵, A. Da Ros²³, A. Dal Molin²⁵, M. Dalla Rosa²⁵, Y. Damizia¹³, O. D'Arcangelo¹⁶, P. David¹⁹, M. De Angeli¹⁴, E. De la Cal²⁸, E. De La Luna²⁸, G. De Tommasi²¹, J. Decker⁷, R. Dejarnac¹⁰, D. Del Sarto³³, G. Derks³⁶, C. Desgranges²³, P. Devynck²³, S. Di Genova⁵⁰, L. E. di Grazia²¹, A. Di Siena¹⁹, M. Dicorato²⁰, M. Diez²³, M. Dimitrova¹⁰, T. Dittmar³⁵, L. Dittrich²⁹, J. J. Domínguez Palacios Durán²⁶, P. Donnel²³, D. Douai²³, S. Dowson¹³, S. Doyle²⁶, M. Dreval⁵¹, P. Drews³⁵, L. Dubus²³, R. Dumont²³, D. Dunaj²⁴, M. Dunne¹⁹, A. Durif²³, F. Durodie³⁹, G. Durr Legoupil Nicoud⁷, B. Duval⁷, R. Dux¹⁹, T. Eich¹⁹, A. Ekedahl²³, S. Elmore¹³, G. Ericsson¹⁸, J. Eriksson¹⁸, B. Eriksson¹⁸, F. Eriksson¹³, S. Ertmer³⁵, A. Escarguel²², B. Esposito¹⁶, T. Estrada²⁸, E. Fable¹⁹, M. Faitsch¹⁹, N. Fakhryi Mofrad¹², A. Fanni²⁷, T. Farley¹³, M. Farník¹⁰, N. Fedorczak²³, F. Felici⁷, X. Feng⁵², J. Ferreira⁴⁰, D. Ferreira⁴⁰, N. Ferron⁹, O. Fevrier⁷, O. Ficker¹⁰, A. R. Field¹³, A. Figueiredo⁴⁰, N. Fil¹³, D. Fiorucci¹⁶, M. Firdaouss²³, R. Fischer¹⁹, M. Fitzgerald¹³, M. Flebbe³⁵, M. Fontana¹³, J. Fontdecaba Climent²⁸, A. Frank⁷, E. Fransson⁵³, L. Frassinetti²⁹, D. Frigione⁴³, S. Futatani³², R. Futtersack¹³, S. Gabriellini⁵⁴, D. Gadariya²⁸, D. Galassi⁷, K. Galazka⁴⁵, J. Galdon²⁶, S. Galeani⁴³, D. Gallart³², A. Gallo²³, C. Galperti⁷, M. Gambrioli⁹, S. Garavaglia¹⁴, J. Garcia²³, M. Garcia Munoz²⁶, J. Gardarein²⁰, L. Garzotti¹³, J. Gaspar⁵⁵, R. Gatto⁵⁴, P. Gaudio⁴³, M. Gelfusa⁴³, J. Gerardin²³, S. N. Gerasimov¹³, R. Gerru Miguelanez⁵⁶, G. Gervasini¹⁴, Z. Ghani¹³, F. M. Ghezzi¹⁴, G. Ghillardi¹⁶, L. Giannone¹⁹, S. Gibson¹³, L. Gil⁴⁰, A. Gillgren⁵³, E. Giovannozzi¹⁶, C. Giroud¹³, G. Giruzzi²³, T. Gleiter¹⁹, M. Gobbin⁹, V. Goloborodko⁵⁷, A. González Ganzábal²⁸, T. Goodman⁷, V. Gopakumar¹³, G. Gorini²⁵, T. Görler¹⁹, S. Gorno⁷, G. Granucci¹⁴, D. Greenhouse⁴⁸, G. Grenfell¹⁹, M. Griener¹⁹, W. Gromelski⁴⁵, M. Groth¹², O. Grover^{10,19}, M. Gruca⁴⁵, A. Gude¹⁹, C. Guillemaut²³, R. Guirlet²³, J. Gunn²³, T. Gyergyek⁴⁷, L. Hagg¹⁸, A. Hakola⁵⁸, J. Hall¹⁵, C. J. Ham¹³, M. Hamed³⁶, T. Happel¹⁹, G. Harrer⁵⁹, J. Harrison¹³, D. Harting³⁵, N. C. Hawkes¹³, P. Heinrich¹⁹, S. Henderson¹³, P. Hennequin⁶⁰, R. Henriques¹³, S. Heurax³⁸,

J. Hidalgo Salaverri²⁶, J. Hillairet²³, J. C. Hillesheim¹³, A. Hjalmarsson¹⁸, A. Ho³⁶, J. Hobirk¹⁹, E. Hodille²³, M. Hölzl¹⁹, M. Hoppe^{7,29}, J. Horacek¹⁰, N. Horsten⁴², L. Horvath¹³, M. Houry²³, K. Hromasova¹⁰, J. Huang³⁵, Z. Huang¹³, A. Huber³⁵, E. Huett⁷, P. Huynh²³, A. Iantchenko⁷, M. Imrisek¹⁰, P. Innocente⁹, C. Ionita Schrittwieser⁶¹, H. Isliker⁶², P. Ivanova⁶³, I. Ivanova Stanik⁴⁵, M. Jablczynska⁴⁵, S. Jachmich⁴⁴, A. S. Jacobsen⁵⁶, P. Jacquet¹³, A. Jansen van Vuuren^{7,26}, A. Jardin⁶⁴, H. Järleblad⁵⁶, A. Järvinen⁵⁸, F. Jaulmes¹⁰, T. Jensen⁵⁶, I. Jepu^{13,49}, S. Jessica⁶⁵, E. Joffrin²³, T. Johnson²⁹, A. Juven²³, J. Kalis¹⁹, A. Kappatou¹⁹, J. Karhunen⁵⁸, R. Karimov⁷, A. N. Karpushov⁷, S. Kasilov¹¹, Y. Kazakov³⁹, P. V. Kazantzidis¹⁷, D. Keeling¹³, W. Kernbichler¹¹, H. T. Kim¹³, D. B. King¹³, V. G. Kiptily¹³, A. Kirjasuo⁵⁸, K. K. Kirov¹³, A. Kirschner³⁵, A. Kit⁶⁶, T. Kiviniemi¹², F. Kjær⁵⁶, E. Klinkby⁵⁶, A. Knieps³⁵, U. Knoche³⁵, M. Kochan⁴⁴, F. Köchl¹³, G. Kocsis¹³, J. T. W. Koenders³⁶, L. Kogan¹³, Y. Kolesnichenko⁵⁷, Y. Kominis¹⁷, M. Komm¹⁰, M. Kong⁷, B. Kool³⁶, S. B. Korsholm⁵⁶, D. Kos¹³, M. Koubiti²⁰, J. Kovacic⁴⁷, Y. Kovtun⁵¹, E. Kowalska Strzeciwiłk⁴⁵, K. Koziol⁶⁷, M. Kozulia⁵¹, A. Krämer Flecken³⁵, A. Kreter³⁵, K. Krieger¹⁹, U. Kruezi⁴⁴, O. Krutkin⁷, O. Kudlacek¹⁹, U. Kumar⁷, H. Kumpulainen¹², M. H. Kushoro²⁵, R. Kwiatkowski⁶⁷, M. La Matina⁹, B. Labit⁷, M. Lacquaniti²⁷, L. Laguardia¹⁴, P. Lainer¹¹, P. Lang¹⁹, M. Larsen⁵⁶, E. Laszynska⁴⁵, K. D. Lawson¹³, A. Lazaros¹⁷, E. Lazzaro¹⁴, M. Y. K. Lee⁷, S. Leerink¹², M. Lehnen⁴⁴, M. Lennholm¹³, E. Lerche³⁹, Y. Liang³⁵, A. Lier¹⁹, J. Likonen⁵⁸, O. Linder¹⁹, B. Lipschultz⁴⁸, A. Listopad⁷, X. Litaudon²³, E. Litherland Smith¹³, D. Liuzza¹⁶, T. Loarer²³, P. J. Lomas¹³, J. Lombardo⁹, N. Lonigro⁴⁸, R. Lorenzini⁹, C. Lowry¹³, T. Luda di Cortemiglia¹⁹, A. Ludvig Osipov⁵³, T. Lunt¹⁹, V. Lutsenko⁵⁷, E. Macusova¹⁰, R. Mäenpää¹², P. Maget²³, C. F. Maggi¹³, J. Mailloux¹³, S. Makarov¹⁹, K. Malinowski⁴⁵, P. Manas²³, A. Mancini²⁶, D. Mancini^{7,41}, P. Mantica⁴¹, M. Mantsinen⁶⁸, J. Manyer³², M. Maraschek¹⁹, G. Marceca⁷, G. Marcer¹⁴, C. Marchetto⁶⁹, S. Marchioni⁷, A. Mariani¹⁴, M. Marin⁷, M. Markl¹¹, T. Markovic¹⁰, D. Marocco¹⁶, S. Marsden¹³, L. Martellucci⁴³, P. Martin⁹, C. Martin²², F. Martinelli⁴³, L. Martinelli⁷, J. R. Martin Solis⁷⁰, R. Martone²¹, M. Maslov¹³, R. Masocco⁴³, M. Mattei²¹, G. F. Matthews¹³, D. Matveev³⁵, E. Matveeva¹⁰, M. L. Mayoral¹³, D. Mazon²³, S. Mazzi^{7,20}, C. Mazzotta¹⁶, G. McArdle¹³, R. McDermott¹⁹, K. McKay²⁶, A. G. Meigs¹³, C. Meineri³⁰, A. Mele⁴¹, V. Menkovski⁷¹, S. Menmuir¹³, A. Merle⁷, H. Meyer¹³, K. Mikszuta Michalik⁴⁵, D. Milanesio³⁰, F. Militello¹³, A. Milocco²⁵, I. G. Miron⁴⁹, J. Mitchell¹³, R. Mitteau²³, V. Mitterauer¹⁹, J. Mlynar¹⁰, V. Moiseenko⁵¹, P. Molna⁷, F. Mombelli⁷², C. Monti¹⁶, A. Montisci²⁷, J. Morales²³, P. Moreau²³, J. M. Moret⁷, A. Moro¹⁴, D. Moulton¹³, P. Mulholland⁷¹, M. Muraglia²⁰, A. Murari⁹, A. Muraro¹⁴, P. Muscente⁹, D. Mykytchuk⁷, F. Nabais⁴⁰, Y. Nakeva⁴¹, F. Napoli¹⁶, E. Nardon²³, M. F. Nave⁴⁰, R. D. Nem⁵⁶, A. Nielsen⁵⁶, S. K. Nielsen⁵⁶, M. Nocente²⁵, R. Nouaillietas²³, S. Nowak¹⁴, H. Nyström²⁹, R. Ochoukov¹⁹, N. Offeddu⁷, S. Olasz²⁴, C. Olde¹³, F. Oliva⁴³, D. Oliveira⁷, H. J. C. Oliver¹³, P. Ollus¹², J. Ongena³⁹, F. P. Orsitto¹⁶, N. Osborne¹³, R. Otin¹³, P. Oyola Dominguez²⁶, D. I. Palade⁴⁹, S. Palomba⁴³, O. Pan¹⁹, N. Panadero²⁸, E. Panontin²⁵, A. Papadopoulos¹⁷, P. Papagiannis¹⁷, G. Papp¹⁹, V. V. Parail¹³, C. Pardanaud²⁰, J. Paris⁷³, A. Parrott¹³, K. Paschalidis⁷⁴, M. Passoni⁷², F. Pastore⁷, A. Patel¹³, B. Patel¹³, A. Pau⁷, G. Pautasso¹⁹, R. Pavlichenko⁵¹, E. Pawelec⁶⁷, B. Pegourie²³, G. Pelka⁴⁵, E. Peluso⁴³, A. Perek^{7,36}, E. Perelli Cippo¹⁴, C. Perez Von Thun⁴⁵, P. Petersson²⁹, G. Petravich²⁴, Y. Peysson²³, V. Piergotti¹⁶, L. Pigatto⁹, C. Piron¹⁶, L. Piron⁹, A. Pironti²¹, F. Pisano²⁷, U. Plank¹⁹, B. Ploeckl¹⁹, V. Plyusnin⁴⁰, A. Podolnik¹⁰, Y. Poels^{7,71}, G. Pokol²⁴, J. Poley⁷, G. Por²⁴, M. Poradzinski¹³, F. Porcelli³⁰, L. Porte⁷, C. Possieri⁴³, A. Poulsen⁵⁶, I. Predebon⁹, G. Pucella¹⁶, M. Pueschel³⁶, P. Puglia⁷, O. Putignano²⁵, T. Pütterich¹⁹, V. Quadri²³, A. Quercia²¹, M. Rabinski⁶⁷, L. Radovanovic⁵⁹, R. Ragona⁵⁶, H. Raj⁷, M. Rasinski³⁵, J. Rasmussen⁵⁶, G. Ratta²⁸, S. Ratynskaia⁷⁴, R. Rayaprolu³⁵, M. Rebai¹⁴, A. Redl⁴¹, D. Rees¹², D. Refy²⁴, M. Reich¹⁹, H. Reimerdes⁷, B. C. G. Reman⁵⁶, O. Renders⁴², C. Reux²³, D. Ricci¹⁴, M. Richou²³, S. Rienacker⁶⁰, D. Rigamonti¹⁴, F. Rigollet⁷⁵, F. G. Rimini^{13,76}, D. Ripamonti¹⁴, N. Rispoli¹⁴, N. Rivals²³, J. F. Rivero Rodriguez²⁶, C. Roach¹³, G. Rocchi¹⁶, S. Rode^{35,37}, P. Rodrigues⁴⁰, J. Romazanov³⁵, C. F. Romero Madrid²⁶, J. Rosato²⁰, R. Rossi⁴³, G. Rubino¹⁶, J. Rueda Rueda²⁶, J. Ruiz Ruiz⁷³, P. Ryan¹³, D. Ryan¹³, S. Saarelma¹³, R. Sabot²³, M. Salewski⁵⁶, A. Salmi⁵⁸, L. Sanchis¹², A. Sand¹², J. Santos⁴⁰, K. Särkimäki¹⁹, M. Sassano⁴³, O. Sauter⁷, G. Schettini⁷⁷, S. Schmuck¹⁴, P. Schneider¹⁹, N. Schoonheere²³, R. Schramm¹⁹, R. Schrittwieser⁶¹, C. Schuster¹⁹, N. Schwarz¹⁹, F. Sciortino¹⁹, M. Scotto D'Abusco²³, S. Scully¹³, A. Selce¹⁴, L. Senni¹⁶, M. Senstius⁵⁶, G. Sergienko³⁵, S. E. Sharapov¹³, R. Sharma¹³, A. Shaw¹³, U. Sheikh⁷, G. Sias²⁷, B. Sieglin¹⁹, S. A. Silburn¹³, C. Silva⁴⁰, A. Silva⁴⁰, D. Silvagni¹⁹, B. Simmendefeldt Schmidt⁵⁶, L. Simons⁷, J. Simpson¹³, L. Singh³⁰, S. Sipilä¹², Y. Siusko⁵¹, S. Smith¹³, A. Snicker⁵⁸, E. R. Solano²⁸, V. Solokha¹², M. Sos¹⁰, C. Sozzi¹⁴, F. Spineanu⁴⁹, G. Spizzo⁹, M. Spolaore⁹, L. Spolladore⁴³, C. Srinivasan¹³, A. Stagni⁹, Z. Stancar¹³, G. Stankunas⁷⁸, J. Stober¹⁹, P. Strand⁵³, C. I. Stuart¹³, F. Subba³⁰, G. Y. Sun⁷, H. J. Sun¹³, W. Suttrop¹⁹, J. Svoboda¹⁰, T. Szepesi²⁴, G. Szepesi¹³, B. Tal¹⁹, T. Tala⁵⁸, P. Tamain²³, G. Tardini¹⁹, M. Tardocchi¹⁴, D. Taylor¹³, G. Telesca⁴⁵, A. Tenaglia⁴³, A. Terra³⁵, D. Terranova⁹, D. Testa⁷, C. Theiler⁷, E. Tholerus¹³, B. Thomas¹³, E. Thoren⁷⁴, A. Thornton¹³, A. Thrysoe⁵⁶, Q. Tichit²³, W. Tierens¹⁹, A. Titarenko⁷⁹, P. Tolias⁷⁴, E. Tomasina⁹, M. Tomes¹⁰, E. Tonello^{7,72}, A. Tookey¹³, M. Toscano Jiménez²⁶, C. Tsironis¹⁷, E. Tsitrone²³, E. Tsitrone²³, C. Tsui^{7,80}, A. Tykhyy⁵⁷, M. Ugoletti⁹, M. Usoltseva¹⁹, D. F. Valcarcel¹³, A. Valentini⁵⁶, M. Valisa⁹, M. Vallar⁷, M. Valovic¹³, S. I. Valvis¹⁷, M. van Berkel³⁶, D. Van Eester³⁹, S. Van Mulders⁷, M. van Rossem⁷, R. Vann⁴⁸, B. Vanovac⁸¹, J. Varela Rodriguez⁷⁰, J. Varje¹², S. Vartanian²³, M. Vecsei²⁴, L. Velarde Gallardo²⁶, M. Veranda⁹, T. Verdier⁵⁶, G. Verdoolaege¹⁵, K. Verhaegh¹³, L. Vermare⁶⁰, G. Verona Rinati⁴³, N. Vianello^{9,82}, J. Vicente⁴⁰, E. Viezzer²⁶, L. Vignitchouk⁷⁴, F. Villone²¹, B. Vincent⁷, P. Vincenzi⁹,

M. O. Vlad⁴⁹, G. Vogel¹⁹, I. Voitsekhovitch¹³, I. Voldiner²⁸, P. Vondracek¹⁰, N. M. T. Vu⁷, T. Vuoriheimo⁶⁶, C. Wade⁵², E. Wang³⁵, T. Wauters⁴⁴, M. Weiland¹⁹, H. Weisen^{7,79}, N. Wendler⁴⁵, D. Weston¹³, A. Widdowson¹³, S. Wiesen³⁵, M. Wiesenberger⁵⁶, T. Wijkamp⁷¹, M. Willensdorfer¹⁹, T. Wilson¹³, M. Wischmeier¹⁹, A. Wojenski⁸³, C. Wuethrich⁷, I. Wyss⁴³, L. Xiang¹³, S. Xu³⁵, D. Yadykin⁵³, Y. Yakovenko⁵⁷, H. Yang²³, V. Yanovskiy¹⁰, R. Yi³⁵, B. Zaar²⁹, G. Zadvitskiy¹⁰, L. Zakharov⁶⁶, P. Zanca⁹, D. Zarzoso²⁰, Y. Zayachuk¹³, J. Zebrowski⁶⁷, M. Zerbini¹⁶, P. Zestanakis¹⁷, C. F. B. Zimmermann¹⁹, M. Zlobinski³⁵, A. Zohar⁴⁷, V. K. Zotta⁵⁴, X. Zou²³, M. Zuin⁹, M. Zurita⁷ & I. Zychor⁶⁷

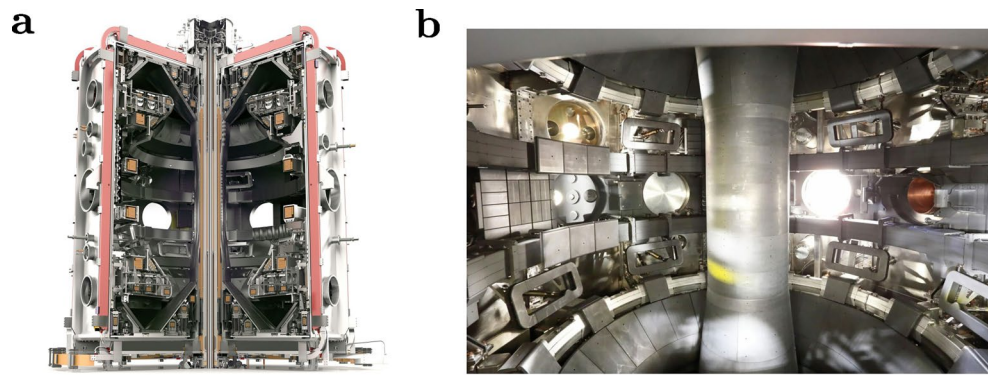
⁹Consorzio RFX (CNR, ENEA, INFN, University of Padova, Acciaierie Venete SpA), Padova, Italy. ¹⁰Institute of Plasma Physics of the CAS, Prague, Czech Republic. ¹¹Graz University of Technology, Graz, Austria. ¹²Aalto University, Aalto, Finland. ¹³United Kingdom Atomic Energy Authority Culham Science Centre, Abingdon, UK. ¹⁴Institute for Plasma Science and Technology, Milan, Italy. ¹⁵Department of Applied Physics, Ghent University, Ghent, Belgium. ¹⁶Dip.to Fusione e Tecnologie per la Sicurezza Nucleare, Rome, Italy. ¹⁷National Technical University of Athens, Athens, Greece. ¹⁸Department of Physics and Astronomy, Uppsala University, Uppsala, Sweden. ¹⁹Max Planck Institute for Plasma Physics, Garching bei München, Germany. ²⁰Aix-Marseille University, CNRS, PIIM UMR 7345, Marseille, France. ²¹Consorzio CREATE, Naples, Italy. ²²Aix Marseille University, CNRS PIIM, Marseille, France. ²³IRFM-CEA Centre de Cadarache, Sant-Paul-lez-Durance, France. ²⁴Centre for Energy Research, Budapest, Hungary. ²⁵University of Milano-Bicocca, Milano, Italy. ²⁶Universidad de Sevilla, Seville, Spain. ²⁷Department of Electrical and Electronic Engineering, University of Cagliari, Cagliari, Italy. ²⁸Laboratorio Nacional de Fusión, CIEMAT Cagliari, Madrid, Spain. ²⁹Electromagnetic Engineering and Fusion Science, EECS, KTH Royal Institute of Technology, Stockholm, Sweden. ³⁰Politecnico di Torino, Torino, Italy. ³¹Dipartimento di Ingegneria Elettrica Elettronica e Informatica, Università degli Studi di Catania, Catania, Italy. ³²Barcelona Supercomputing Center, Barcelona, Spain. ³³Institut Jean Lamour, UMR 7198, CNRS-Université de Lorraine, Vandoeuvre-lès-Nancy, France. ³⁴Institute of Nuclear Physics, Kraków, Poland. ³⁵Forschungszentrum Jülich GmbH, Institut für Energie- und Klimaforschung Plasmaphysik, Jülich, Germany. ³⁶DIFFER-Dutch Institute for Fundamental Energy Research, Eindhoven, Netherlands. ³⁷Faculty of Mathematics and Natural Sciences, Heinrich Heine University Düsseldorf, Düsseldorf, Germany. ³⁸Institut Jean Lamour, Université de Lorraine, Nancy, France. ³⁹Laboratory for Plasma Physics LPP-ERM/KMS, Brussels, Belgium. ⁴⁰Instituto de Plasmas e Fusão Nuclear, Instituto Superior Técnico, Universidade de Lisboa, Lisbon, Portugal. ⁴¹DEIM Department, Università degli Studi della Tuscia, Viterbo, Italy. ⁴²Department of Mechanical Engineering, KU Leuven, Leuven, Belgium. ⁴³Università di Roma Tor Vergata, Rome, Italy. ⁴⁴ITER Organization, Route de Vinon-sur-Verdon, Saint Paul Lez Durance Cedex, France. ⁴⁵Institute of Plasma Physics and Laser Microfusion, Warsaw, Poland. ⁴⁶Astrophysics Research Centre, School of Mathematics and Physics, Queen's University, Belfast, UK. ⁴⁷Jožef Stefan Institute, Ljubljana, Slovenia-University of Ljubljana, Ljubljana, Slovenia. ⁴⁸York Plasma Institute, Department of Physics, University of York, York, UK. ⁴⁹The National Institute for Laser, Plasma and Radiation Physics, Magurele-Bucharest, Romania. ⁵⁰Aix-Marseille University, CNRS M2P2, Marseille, France. ⁵¹National Science Center Kharkov Institute of Physics and Technology, Kharkiv, Ukraine. ⁵²Department of Physics, Durham University, Durham, UK. ⁵³Department of Space, Earth and Environment, SEE, Chalmers University of Technology, Gothenburg, Sweden. ⁵⁴Dipartimento di Ingegneria Astronautica, Elettrica ed Energetica, SAPIENZA Università di Roma, Rome, Italy. ⁵⁵Aix-Marseille University, CNRS, IUSTI UMR 7343, Marseille, France. ⁵⁶Department of Physics, Technical University of Denmark, Kgs Lyngby, Denmark. ⁵⁷Institute for Nuclear Research, Kyiv, Ukraine. ⁵⁸VTT Technical Research Centre of Finland, Espoo, Finland. ⁵⁹Technische Universität Wien, Wien, Austria. ⁶⁰Laboratoire de Physique des Plasmas, Ecole Polytechnique, Palaiseau, France. ⁶¹Institute of Ion Physics and Applied Physics, University of Innsbruck, Innsbruck, Austria. ⁶²Section of Astrophysics, Astronomy and Mechanics, Physics Department, Aristotle University, Thessaloniki, Greece. ⁶³Institute of Electronics, Bulgarian Academy of Sciences (BAS), Sofia, Bulgaria. ⁶⁴Institute of Nuclear Physics Polish Academy of Sciences (IFJ PAN), Krakow, Poland. ⁶⁵Loughborough University, Loughborough, UK. ⁶⁶University of Helsinki, Helsinki, Finland. ⁶⁷National Centre for Nuclear Research (NCBJ), Otwock-Świerk, Poland. ⁶⁸ICREA and Barcelona Supercomputing Center, Barcelona, Spain. ⁶⁹Istituto dei Sistemi Complessi—CNR and Dipartimento di Energia—Politecnico di Torino, Torino, Italy. ⁷⁰Universidad Carlos III de Madrid, Madrid, Spain. ⁷¹Eindhoven University of Technology, Eindhoven, Netherlands. ⁷²Politecnico di Milano, Milan, Italy. ⁷³Rudolf Peierls Centre for Theoretical Physics, University of Oxford, Oxford, UK. ⁷⁴Space and Plasma Physics, EECS KTH, Stockholm, Sweden. ⁷⁵Aix Marseille University, CNRS IUSTI UMR 7343, Marseille, France. ⁷⁶EUROfusion Programme Management Unit, Garching, Germany. ⁷⁷University Roma Tre, Rome, Italy. ⁷⁸Lithuanian Energy Institute, Laboratory of Nuclear Installation Safety, Kaunas, Lithuania. ⁷⁹V.N. Karazin Kharkiv National University, Kharkiv, Ukraine. ⁸⁰Center for Energy Research (CER), University of California-San Diego (UCSD), La Jolla, CA, USA. ⁸¹Massachusetts Institute of Technology, Plasma Science and Fusion Center, Cambridge, MA, USA. ⁸²Istituto per la Scienza e la Tecnologia dei Plasm, CNR, Padova, Italy. ⁸³Warsaw University of Technology, Warsaw, Poland.

the MAST-U team

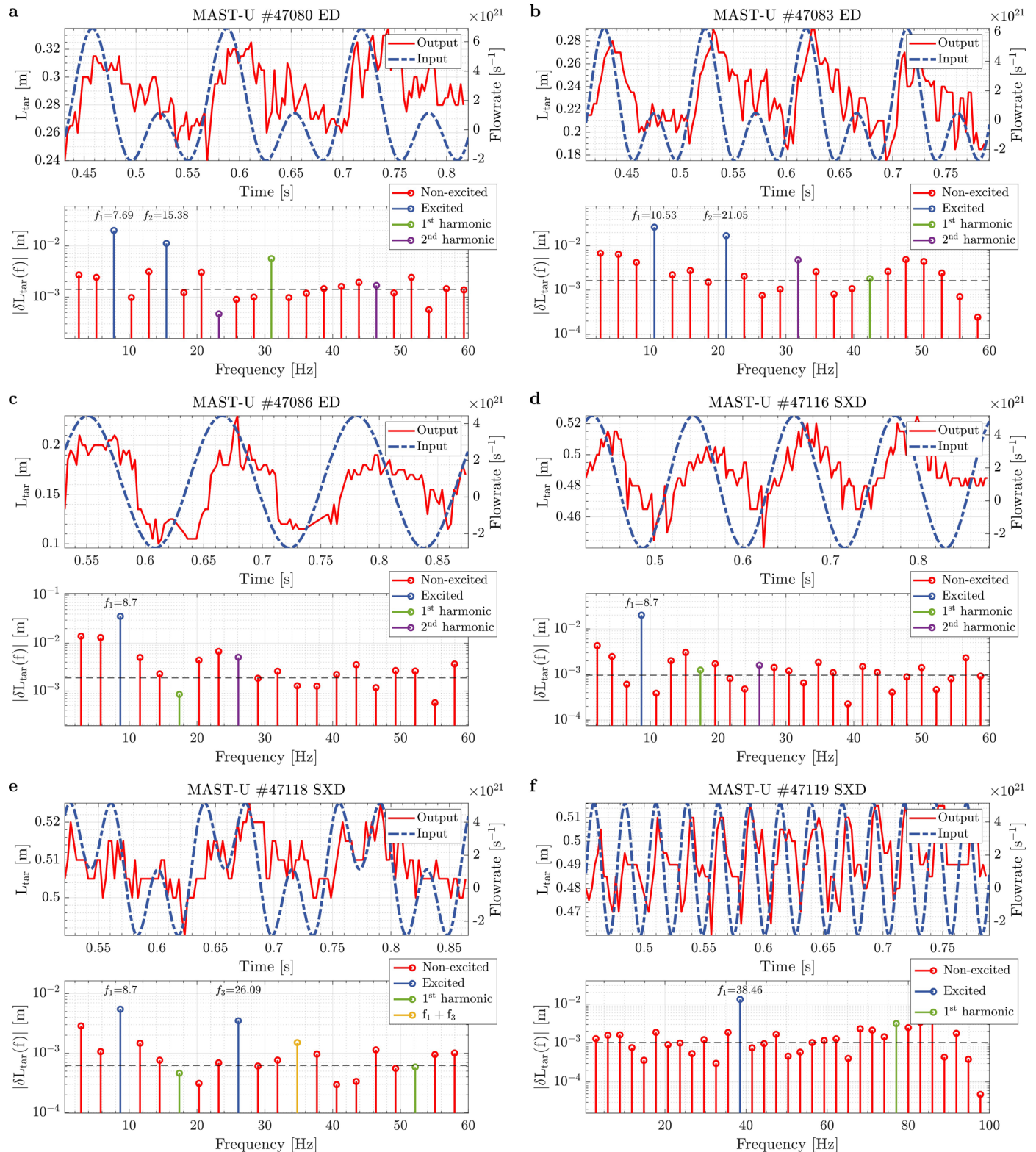
J. R. Harrison¹³, A. Aboutaleb⁸⁴, S. Ahmed⁸⁵, M. Aljunid¹³, S. Y. Allan¹³, H. Anand⁸⁶, Y. Andrew⁸⁷, L. C. Appel¹³, A. Ash¹³, J. Ashton¹³, O. Bachmann¹³, M. Barnes⁷³, B. Barrett¹³, D. Baver⁸⁸, D. Beckett¹³, J. Bennett¹³, J. Berkery⁸⁹, M. Bernert⁶, W. Boeglin⁸⁴, C. Bowman¹³, J. Bradley⁹⁰, D. Brida⁶, P. K. Browning⁹¹, D. Brunetti¹³, P. Bryant⁹⁰, J. Bryant⁹⁰, J. Buchanan¹³, N. Bulmer¹³, A. Carruthers¹³, M. Cecconello⁵², Z. P. Chen⁹², J. Clark^{13,90}, C. Cowley⁹³, M. Coy¹³, N. Crocker⁹⁴, G. Cunningham¹³, I. Cziegler⁹³, T. Da Assuncao¹³, Y. Damizia⁹⁰, P. Davies¹³, I. E. Day¹³, G. L. Derks^{71,95}, S. Dixon¹³, R. Doyle⁹⁶, M. Dreval⁹⁷, M. Dunne⁶, B. P. Duval⁹⁸, T. Eagles¹³, J. Edmond¹³, H. El-Haroun¹³, S. D. Elmore¹³, Y. Enters⁹³, M. Faitsch⁶, F. Federici⁵, N. Fedorczak⁹⁹, F. Felici⁹⁸, A. R. Field¹³, M. Fitzgerald¹³, I. Fitzgerald¹³, R. Fitzpatrick⁹², L. Frassinetti¹⁰⁰, W. Fuller¹⁰¹, D. Gahle¹⁰², J. Galdon-Quiroga¹⁰³, L. Garzotti¹³, S. Gee¹³, T. Gheorghiu⁹³, S. Gibson¹³, K. J. Gibson⁹³, C. Giroud¹³, D. Greenhouse⁹³, V. H. Hall-Chen¹⁰⁴, C. J. Ham¹³, R. Harrison¹³, S. S. Henderson¹³, C. Hickling^{13,90}, B. Hnat¹⁰¹, L. Howlett⁹³, J. Hughes¹⁰⁵, R. Hussain¹³, K. Imada⁹³, P. Jacquet¹³, P. Jepson¹³, B. Kandan¹³, I. Katramados¹³, Y. O. Kazakov¹⁰⁶, D. King¹³, R. King¹³, A. Kirk¹³, M. Knolker⁸⁶, M. Kochan¹³, L. Kogan¹³, B. Kool^{71,95}, M. Kotschenreuther⁹², M. Lees¹³, A. W. Leonard⁸⁶, G. Liddiard¹³, B. Lipschultz⁹³, Y. Q. Liu⁸⁶, B. A. Lomanowski⁵, N. Lonigro⁹³, J. Lore⁵, J. Lovell⁵, S. Mahajan⁹², F. Maiden⁹³, C. Man-Friel¹³, F. Mansfield¹³, S. Marsden¹³, R. Martin¹³, S. Mazzi⁹⁸, R. McAdams¹³, G. McArdle¹³, K. G. McClements¹³, J. McClenaghan⁸⁶, D. McConville¹³, K. McKay⁹⁰, C. McKnight¹³, P. McKnight¹³, A. McLean¹⁰⁷, B. F. McMillan¹⁰¹, A. McShee¹³, J. Measures¹³, N. Mehay¹³, C. A. Michael⁹⁴, F. Militello¹³, D. Morbey¹³, S. Mordijk¹⁰⁸,

D. Moulton¹³, O. Myatra¹³, A. O. Nelson¹⁰⁹, M. Nicassio¹³, M. G. O'Mullane¹⁰², H. J. C. Oliver¹³, P. Ollus¹¹⁰, T. Osborne⁸⁶, N. Osborne⁹⁰, E. Parr¹³, B. Parry¹³, B. S. Patel¹³, D. Payne¹³, C. Paz-Soldan¹⁰⁹, A. Phelps¹⁰², L. Piron^{111,112}, C. Piron¹¹³, G. Prechel¹¹⁴, M. Price¹³, B. Pritchard⁹³, R. Proudfoot¹³, H. Reimerdes⁹⁸, T. Rhodes⁹⁴, P. Richardson¹³, J. Riquezes¹⁰⁹, J. F. Rivero-Rodriguez¹³, C. M. Roach¹³, M. Robson¹³, K. Ronald¹⁰², E. Rose¹³, P. Ryan¹³, D. Ryan¹³, S. Saarelma¹³, S. Sabbagh¹⁰⁹, R. Sarwar¹³, P. Saunders¹³, O. Sauter⁹⁸, R. Scannell¹³, T. Schuett⁹³, R. Seath¹³, R. Sharma¹³, P. Shi¹³, B. Sieglin⁶, M. Simmonds¹³, J. Smith¹³, A. Smith¹³, V. A. Soukhanovskii¹⁰⁷, D. Speirs¹⁰², G. Staebler⁸⁶, R. Stephen¹³, P. Stevenson¹³, J. Stobbs¹³, M. Stott¹³, C. Stroud¹³, C. Tame¹³, C. Theiler⁹⁸, N. Thomas-Davies¹³, A. J. Thornton¹³, M. Tobin¹⁰⁹, M. Vallar⁹⁸, R. G. L. Vann⁹³, L. Velarde¹¹⁵, K. Verhaegh¹³, E. Viezzer¹⁰³, C. Vincent¹³, G. Voss¹³, M. Warr¹³, W. Wehner⁸⁶, S. Wiesen¹¹⁶, T. A. Wijkamp^{71,95}, D. Wilkins¹³, T. Williams¹³, T. Wilson¹³, H. R. Wilson^{5,93}, H. Wong⁹⁴, M. Wood¹³ & V. Zamkovska¹⁰⁹

⁸⁴Department of Physics, Florida International University, Miami, FL, USA. ⁸⁵Department of Physics and Technology, UiT The Arctic University of Norway, Tromsø, Norway. ⁸⁶General Atomics, San Diego, CA, USA. ⁸⁷Blackett Laboratory, Imperial College London, London, UK. ⁸⁸Astrodel LLC, Boulder, CO, USA. ⁸⁹Princeton Plasma Physics Laboratory, Princeton, NJ, USA. ⁹⁰Department of Electrical Engineering and Electronics, University of Liverpool Brownlow Hill, Liverpool, UK. ⁹¹Department of Physics and Astronomy, University of Manchester, Manchester, UK. ⁹²Institute for Fusion Studies, The University of Texas at Austin, Austin, TX, USA. ⁹³York Plasma Institute, Department of Physics, University of York, Heslington, UK. ⁹⁴Physics and Astronomy Department, University of California, Los Angeles, CA, USA. ⁹⁵Dutch Institute for Fundamental Energy Research DIFFER, Eindhoven, Netherlands. ⁹⁶Dublin City University, Dublin, Ireland. ⁹⁷National Science Center 'Kharkov Institute of Physics and Technology', Kharkiv, Ukraine. ⁹⁸Ecole Polytechnique Fédérale de Lausanne (EPFL), Swiss Plasma Center (SPC), Lausanne, Switzerland. ⁹⁹CEA, IRFM F-13108, Saint-Paul-lez-Durance, France. ¹⁰⁰Division of Fusion Plasma Physics, KTH Royal Institute of Technology, Stockholm, Sweden. ¹⁰¹Department of Physics, University of Warwick, Coventry, UK. ¹⁰²Department of Physics, SUPA, University of Strathclyde, Glasgow, UK. ¹⁰³Dpto. de Física Atómica, Molecular y Nuclear, Universidad de Sevilla, Seville, Spain. ¹⁰⁴IHPC, Agency for Science, Technology and Research (A*STAR), Singapore, Singapore. ¹⁰⁵Plasma Science and Fusion Center, Massachusetts Institute of Technology, Cambridge, MA, USA. ¹⁰⁶Laboratory for Plasma Physics, LPP-ERM/KMS, TEC Partner, Brussels, Belgium. ¹⁰⁷Lawrence Livermore National Laboratory, Livermore, CA, USA. ¹⁰⁸Department of Computer Science, College of William and Mary, Williamsburg, VA, USA. ¹⁰⁹Department of Applied Physics and Applied Mathematics, Columbia University, New York, NY, USA. ¹¹⁰Department of Applied Physics, Aalto University, Aalto, Finland. ¹¹¹Dipartimento di Fisica 'G. Galilei', Università degli Studi di Padova, Padova, Italy. ¹¹²Consorzio RFX, Padova, Italy. ¹¹³ENEA, Fusion and Nuclear Safety Department, Rome, Italy. ¹¹⁴University of California Irvine, Irvine, CA, USA. ¹¹⁵Dpto. de Ingeniería Energética, ETSI, Universidad de Sevilla, Seville, Spain. ¹¹⁶Forschungszentrum Jülich GmbH, Institut für Energie- und Klimaforschung—Plasmaphysik, Jülich, Germany.

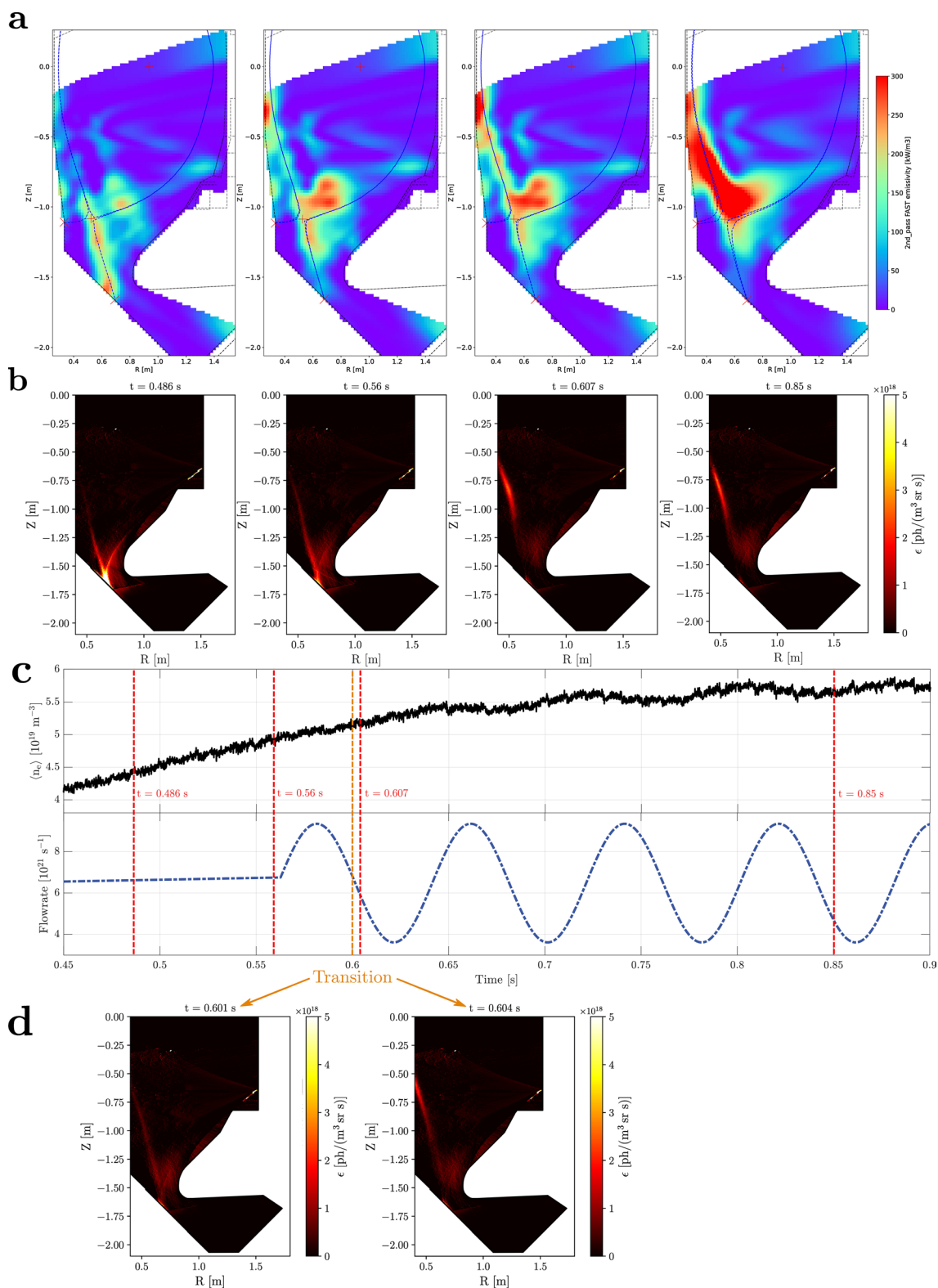


Extended Data Fig. 1 | The MAST-U tokamak. a Cross section of a CAD render of MAST-U. **b** Picture of the interior of MAST-U. Credit: **a, b**, United Kingdom Atomic Energy Authority.



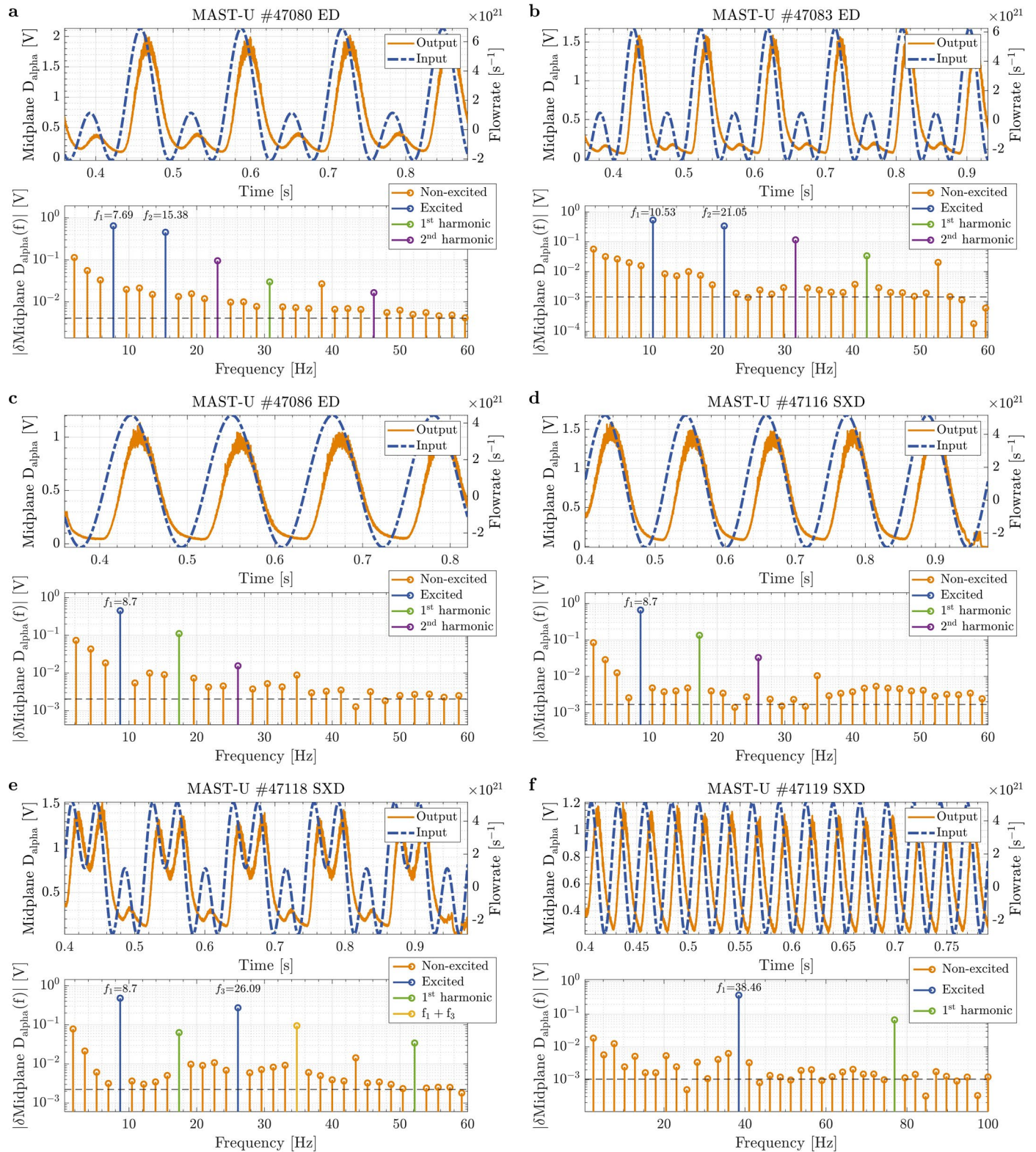
Extended Data Fig. 2 | Detachment front response in MAST-U. Observed time and frequency domain D_2 Fulcher band front position L_{tar} (-) response to main chamber D_2 gas valve flow request perturbations (-). **a-c**, Elongated divertor geometry (#47080, #47083, #47086). **d-f**, Super-X divertor geometry. The excited frequencies and their harmonics are indicated through colour coding.

The output response at the excited frequencies is well above the average noise level of the non-excited frequencies (-). Some response can occasionally be observed at the harmonic frequencies which indicates non-linear components are present⁴⁹, nevertheless, the response is dominantly linear.



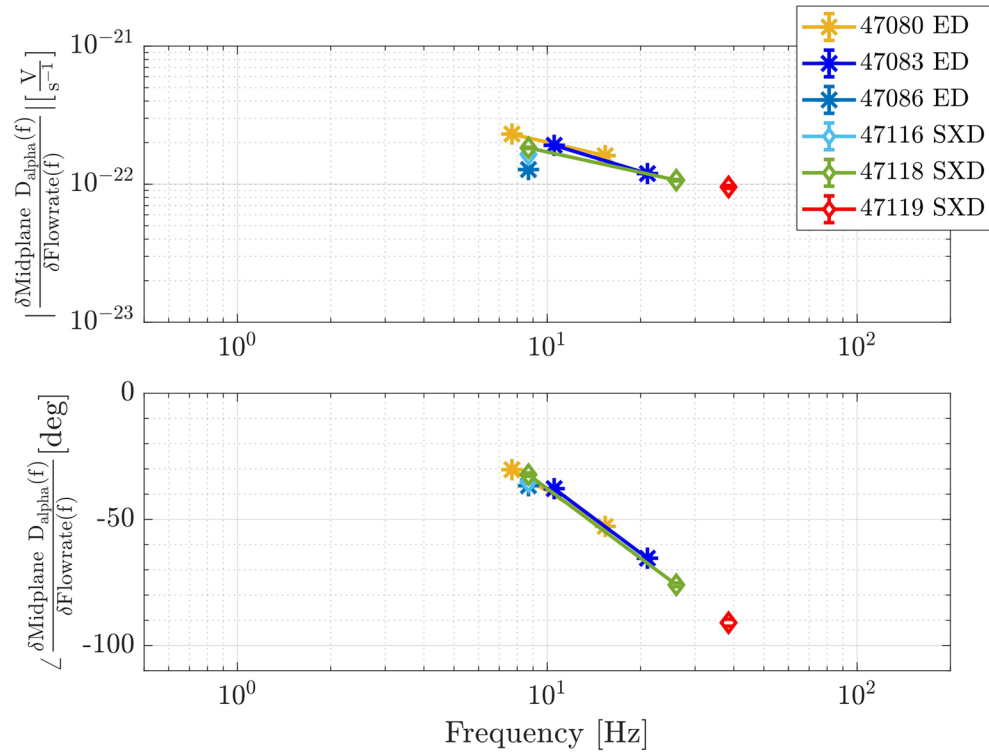
Extended Data Fig. 3 | Conventional divertor front movement experiment #49303. **a** Progression of total radiation location as measured by the infrared video bolometer (IRVB⁶⁷) indicating a transition from mainly attached radiation near the strikepoint to volumetric radiation above the X-point at the high-field-side. The time basis was adapted to match the other instruments; the bright feature on the central column at $z \approx -0.3$ is an artefact of the inversion and not yet a MARFE⁶⁸. **b** Molecular D₂ Fulcher band emission inversions from the MWI⁴⁴ and X-point imaging systems, showing how the front position transitions from

attached to above the X-point at the high-field side. **c** Line-averaged electron density and requested main chamber gas flow rate with the timestamps of the radiation and emission plots indicated as well as the approximate time of transition from attached D₂ Fulcher band emission to above the X-point. **d** Two consecutive Fulcher band emission inversions around the transition point, indicating how the transition from attached emission to above the X-point occurs within one acquisition window (2.5 ms).

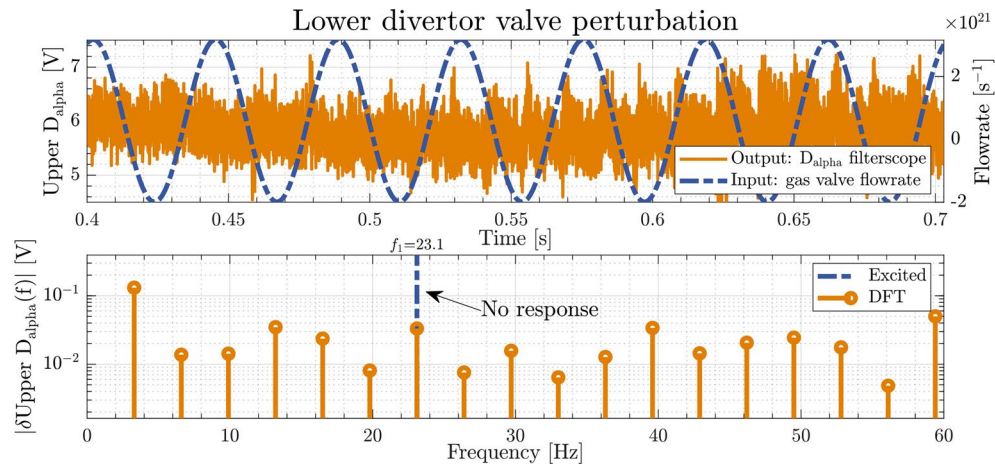


Extended Data Fig. 4 | Main chamber gas valve response in MAST-U. Observed time and frequency domain response of the HM10ET midplane D_{α} filterscope (-) to main chamber D_2 gas valve flow request perturbations (-). **a-c**, Elongated divertor geometry (#47080, #47083, #47086). **d-f**, Super-X divertor geometry.

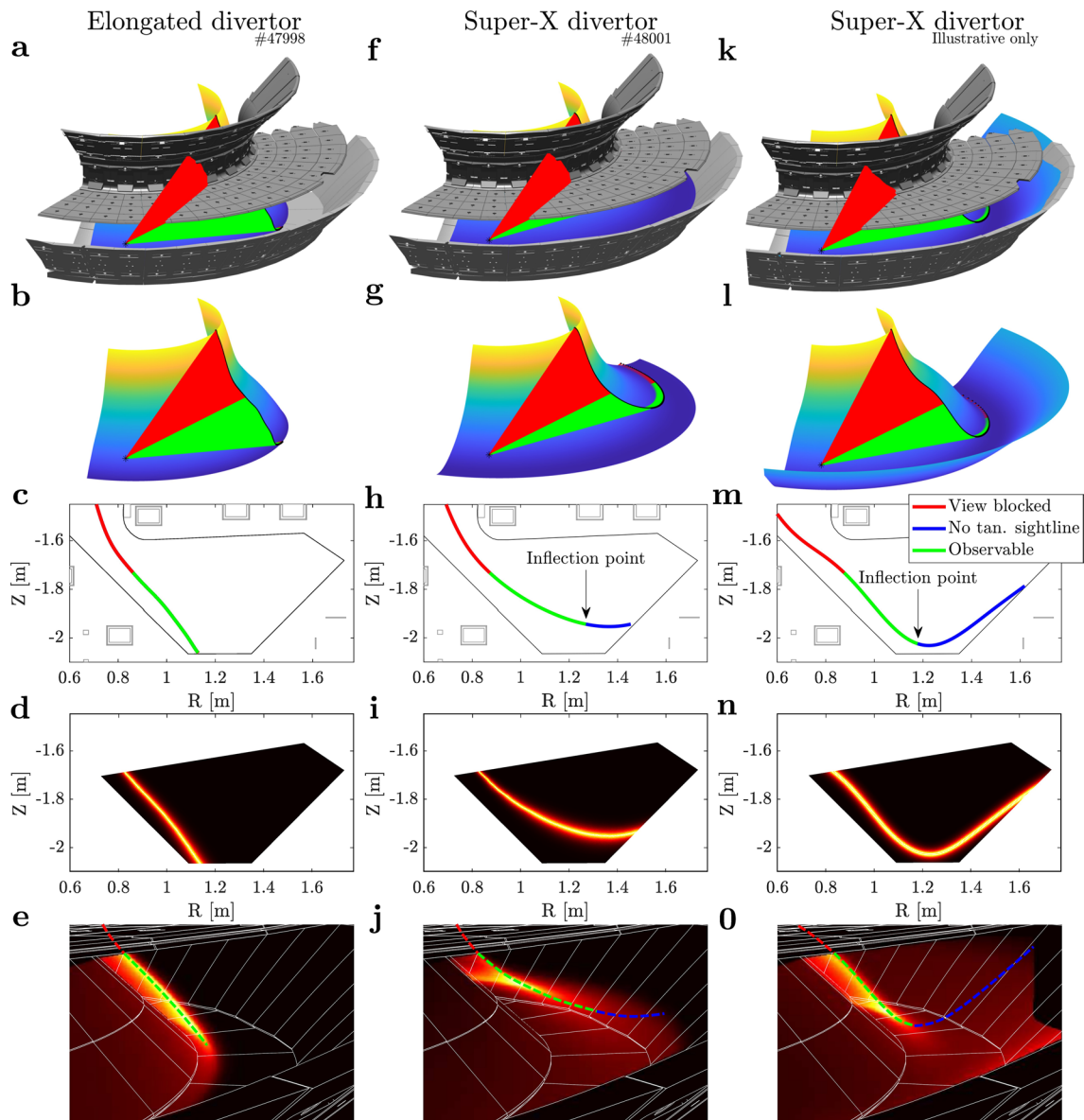
The excited frequencies and their harmonics are indicated through colour coding. The high signal-to-noise ratio leads to a low average noise level of the non-excited elongated frequencies (-), allowing the response at the harmonic frequencies which originates from non-linear components to be clearly identified⁴⁹.



Extended Data Fig. 5 | Midplane D_{α} frequency response. Requested main chamber gas valve flow rate change to HM10ET midplane D_{α} filterscope response in Elongated (*) and Super-X (◇) configuration expressed as gain and phase ratio over frequency. Mean response value and 2σ error bars obtained using the LPM^{47,49} across 4 (#47080, #47086), 5 (#47116, #47118), 6 (#47083), and 15 periods (#47119).



Extended Data Fig. 6 | Upper divertor D_{α} response to lower divertor valve perturbation in experiment #49297. Time domain and frequency domain response of the detrended upper divertor D_{α} filterscope (-) around the operating point to a perturbation of the requested lower D_2 divertor gas valve flow rate (-).



Extended Data Fig. 7 | Geometric analysis and synthetic MWI camera images to quantify the observable region for front tracking. Shown are the Elongated (a–e) and Super-X (f–j) divertor geometries employed in the experiments shown in this paper as well as a purely synthetic Super-X divertor variant (k–o) for illustrative purposes. a, f, k Separatrix surface, MAST-U divertor CAD model, and the observable (green) and blocked (red) MWI camera sightlines. b, g, l Removed CAD model for increased visibility. c, h, m Poloidal view of the observable (green) and blocked (red) parts of the divertor leg, the regions where no tangential sightline exists are indicated in blue. d, i, n The synthetic poloidal emission

profiles assumed for generating synthetic images, emissivity is assumed along the entire divertor leg. e, j, o Synthetic divertor images generated using the assumed poloidal divertor emission, employing the CALCAM⁸³ software package, with divertor CAD model overlay. The geometric analysis results (c, h, m) are overlaid approximately on the synthetic images (e, j, o) to highlight their interconnection: a tangential sightline is required to observe the divertor leg on the images. The location of the inflection point therefore greatly influences the observable region, as is evident from comparing both Super-X divertor variants.



Extended Data Fig. 8 | The STEP tokamak. Artistic impression of the Spherical Tokamak for Energy Production (STEP) concept design. Credit: UK Industrial Fusion Solutions.